This is a preprint, the final version is subject to change, of the American Mineralogist (MSA)
Cite as Authors (Year) Title. American Mineralogist, in press.
DOI: https://doi.org/10.2138/am-2018-6543

Revision 1

High-pressure granulite facies metamorphism (~1.8 GPa) revealed in silica-undersaturated garnet-spinel-corundum gneiss, Central Maine Terrane, Connecticut, U.S.A.

Duncan S. Keller and Jay J. Ague

Department of Geology and Geophysics

Yale University

PO Box 208109

New Haven, CT 06520-8109 USA

duncan.keller@yale.edu

This is a preprint, the final version is subject to change, of the American Mineralogist (MSA)
Cite as Authors (Year) Title. American Mineralogist, in press.
DOI: https://doi.org/10.2138/am-2018-6543

ABSTRACT

We quantify the metamorphic pressure-temperature (*P-T*) conditions for a newly discovered silica-undersaturated high-pressure granulite (HPG) from the Central Maine Terrane (CMT) in northeastern Connecticut, United States. The rocks lie within the Acadian-Neoacadian orogenic belt (Devonian) and form part of the Brimfield Schist. The Brimfield and the adjacent Bigelow Brook Formation contain silica-saturated rocks that have previously been shown to have undergone ~1000 ^{o}C metamorphism. Pressure was less well constrained at ≥ ~1 GPa. Silica-undersaturated rocks hold underutilized potential for pinpointing peak metamorphic conditions, particularly pressure, because of their resilience to melting and the variety of refractory minerals they contain. The typical silica-undersaturated mineral assemblage is garnet + spinel + corundum + plagioclase + K-feldspar + biotite + ilmenite. Leucosomes are syenites consisting of two feldspars ± biotite. Plagioclase is commonly antiperthitic, particularly in feldspathic domains surrounding peritectic garnet; such garnet crystals reach ~10 cm in diameter. Alkali feldspars are perthitic. The rocks contain remarkable ellipsoidal spinels as much as 5.5 cm long comprising discrete crystallographic domains hosting crystallographically oriented lamellae of a Fe-Ti phase, most likely ilmenite. Corundum is usually colorless, but can also be found as sapphire in shades of pink, purple, and blue, particularly in antiperthite-rich domains surrounding large garnets. Some sapphires are concentrically color zoned. We carried out *P-T* estimation using ternary feldspar reintegration thermometry of metamorphic antiperthites together with pseudosection modeling. Samples texturally and chemically record near-eclogite facies equilibration at minimum conditions of ~1040 °C and ~1.8 GPa, establishing the CMT in northeastern CT as the first known HPG locality in the United States. These results are consistent with high P_2O_5 levels found in garnet (0.18 wt%), Ti-in-biotite thermometry, regional sillimanite

This is a preprint, the final version is subject to change, of the American Mineralogist (MSA)
Cite as Authors (Year) Title. American Mineralogist, in press.
DOI: https://doi.org/10.2138/am-2018-6543

pseudomorphs after kyanite, and preliminary experimental work on melt inclusions in garnet (Ferrero et al. 2017). The leucosomes provide strong evidence that partial melting of silica-undersaturated rocks at HPG conditions can produce syenitic magmata. Strongly melt-depleted silica-undersaturated rocks may also be protoliths for garnet + spinel + corundum xenoliths reported from kimberlites. The presence of HPG gneisses demonstrates that the large-scale thrusts of the CMT sample the deepest roots of the orogenic belt (60–70 km), and perhaps even deeper subduction zone lithologies as well.

Keywords: High-pressure granulite, silica-undersaturated, corundum, spinel, garnet

INTRODUCTION

High-pressure granulites (HPG) form at or below the base of orogenically thickened crust at pressures (P) ≥1.5 GPa and temperatures (T) ≥850 °C in the stability field of kyanite, commonly at eclogite facies conditions (O'Brien and Rötzler 2003). They provide textural, chemical, and mineralogical records of lower crustal processes and environments, and are particularly valuable tools for evaluating models of how mountain belts form, the depths to which continental material can be underthrust and potentially subducted, and how rocks are exhumed from deep crustal levels. Although HPGs are reported from many orogenic belts worldwide (see O'Brien and Rötzler 2003, Kotková 2007, and references therein) none have been identified in the United States of America. Paleoproterozoic HPGs are present in the Snowbird tectonic zone of Canada (Snoeyenbos et al. 1995; Baldwin et al. 2003), and Neoproterozoic HPGs (and eclogites) are present in the Grenville orogen of eastern Canada (Indares 1993; Indares 1995; Indares 1997; Indares et al. 1998; Indares and Dunning 2001). The lack of high-pressure granulites in the northeastern United States is particularly conspicuous, as granulites are a significant component of the Acadian-Neoacadian orogen in the Central Maine

This is a preprint, the final version is subject to change, of the American Mineralogist (MSA)
Cite as Authors (Year) Title. American Mineralogist, in press.
DOI: https://doi.org/10.2138/am-2018-6543

Terrane (Peper and Pease 1975; Fahey and Pease 1977; Chamberlain and England 1985; Schumacher et al. 1989; Robinson et al. 1998).

Recent experimental evidence suggests, however, that silicic ultrahigh-temperature granulites of the Brimfield Schist and Upper Member of the Bigelow Brook Formation in northeastern Connecticut, part of the Central Maine Terrane (Ague et al. 2013; Axler and Ague 2015a) underwent early HPG metamorphism (Ferrero et al. 2017). Re-homogenization of quartz-bearing melt inclusions indicates that for T 1050 °C (Axler and Ague 2015a), melt entrapment occurred at $P \geq 1.7$ GPa (Ferrero et al. 2017). These conditions exceed the canonical pressure limit of UHT metamorphism (Harley 1998; Brown 2006; Kelsey 2008) and easily reach the high-pressure granulite facies. This result is preliminary, but nonetheless offers a tantalizing glimpse of higher-pressure metamorphism than has been previously reported in the orogen.

Independent corroboration of this P estimate is necessary to establish the nature and extent of HPG metamorphism within the orogen. However, the matrix assemblage of the quartz-bearing granulites does not provide a robust pressure constraint other than the rutile/ilmenite transition, yielding minimum P ~1 GPa (Ague et al. 2013). Distinguishing ultrahigh-temperature (UHT) rocks from HPGs represents a particular challenge because unless HPG indicator minerals like kyanite form and are preserved, many intermediate and felsic bulk compositions crystallize quartzofeldspathic garnet-bearing assemblages that are not strongly diagnostic of pressure at ~1000 °C and 1–2 GPa. In fact, the type locality granulites from the Granulitgebirge of Saxony, Germany were only recently recognized as HPGs, based on petrographic observations coupled with modern geothermobarometric and modeling techniques (e.g. Rötzler 1992; Rötzler and Romer 2001; O'Brien 2006; Müller et al. 2015). Silica-undersaturated rocks, however, have

This is a preprint, the final version is subject to change, of the American Mineralogist (MSA)
Cite as Authors (Year) Title. American Mineralogist, in press.
DOI: https://doi.org/10.2138/am-2018-6543

the potential to provide independent *P-T* constraints at UHT and HPG conditions (e.g. Kelsey et al. 2005; Kelsey 2008; Dorfler et al. 2015; Guevara and Caddick 2016).

In particular, silica-undersaturated rocks that contain coexisting garnet, spinel, and corundum hold significant promise for revealing *P-T* histories. Such rocks are not commonly described in the literature, but are nonetheless reported from a number of field areas worldwide including in India (Harris 1981; Sengupta et al. 1999; Shimpo et al. 2006), Sri Lanka (Osanai et al. 2006; Dharmapriya et al. 2015), Algeria (Ouzegane et al. 2003), South Africa (Schreyer et al. 1984), Antarctica (Asami et al. 1989; Asami et al. 1990), the United States (Cortland complex; e.g. Dorfler et al. 2014, 2015), and Canada (Snoeyenbos et al. 1995). Roof pendants in the Vinalhaven pluton (Maine, U.S.A.) contain garnet, spinel, and corundum, but these minerals do not form a distinct assemblage; garnet is only present in leucosomes with quartz (Porter et al. 1999). Retrogressed eclogite from the Trans-Hudson orogen contains garnet with spinel ± corundum (+ plagioclase) symplectites after kyanite (Weller and St-Onge 2017). Kimberlite pipes have yielded bi- to tri-mineralic garnet ± spinel ± corundum xenoliths which can contain cm-scale colored corundum and are generally interpreted as mantle cumulates or extremely melt-depleted metapelites sourced from slabs (Nixon et al. 1978; Padovani and Tracy 1981; Exley et al. 1983; Mazzone and Haggerty 1989).

In this paper, we describe a newly discovered silica-undersaturated lithology from the Central Maine Terrane, Connecticut (CT), which contains porphyroblastic garnet, spinel, and corundum. The rocks are part of the same litho-tectonic rock sequence in which Ague et al. (2013) and Axler and Ague (2015a) determined extreme metamorphic $T \sim 1000\ ^{o}C$. We evaluate equilibration *P-T* conditions using ternary feldspar reintegration thermometry and pseudosection modeling in conjunction with textural observations. The results demonstrate that the rocks

reached HPG conditions, the first *in-situ* HPG example we are aware of in the United States. If the silica-saturated rocks studied by Axler and Ague (2015a) and Ferrero et al. (2017) are also HPG, then multiple HPG localities exist in the Central Maine Terrane. We then discuss the tectonic implications of HPG rocks within the Central Maine Terrane and the potential of these rock types to elucidate lower crustal processes.

GEOLOGIC SETTING

The Brimfield Schist hosts the rocks of this study and is one of several rock units cut and/or bounded by west-northwest-dipping thrust faults within the southern Central Maine Terrane (CMT; also known as, for example, the Merrimack Synclinorium, e.g. Rodgers 1981, and the Central Maine belt, e.g. Robinson et al. 1998). Together with the other rock units in this area it reached or exceeded granulite facies metamorphic conditions (Tracy et al. 1976; Robinson 1978; Rodgers 1981; Ague et al. 2013) (Figure 1). The Brimfield Schist and its internal shear zones contain a wide variety of lithologies including aluminous and quartzofeldspathic gneisses, granitoids, amphibolites, ultramafic blocks, rare metacarbonate rocks, and the silica-undersaturated rocks described herein (Ague et al. 2013).

Silica-saturated metapelitic gneisses of the Brimfield Schist and the adjacent Bigelow Brook Formation record a UHT signature (Ague et al. 2013; Axler and Ague 2015a). These rocks locally preserve a matrix assemblage with spinel and cordierite from this phase of metamorphism, stable at ~0.6 GPa. As noted above, however, recent melt-inclusion re-homogenization experiments show that a HPG stage (~1050°C; 1.7–2.0 GPa) likely pre-dated UHT metamorphism in the Bigelow Brook Formation (Ferrero et al. 2017). Sillimanite pseudomorphs after kyanite are preserved in metapelitic gneisses of the Brimfield Schist and Bigelow Brook Formation (Peper and Pease 1975; Fahey and Pease 1977; Axler and Ague

This is a preprint, the final version is subject to change, of the American Mineralogist (MSA)
Cite as Authors (Year) Title. American Mineralogist, in press.
DOI: https://doi.org/10.2138/am-2018-6543

2015a). This is consistent with overprinting of kyanite-bearing HPG assemblages by later, lower-pressure, UHT metamorphism.

Additional metamorphic overprints have affected the region. A 700–800 ^{o}C, 0.5–0.6 GPa granulite facies signature was recognized by Ague et al. (2013) as post-dating the UHT signature of quartz-bearing metapelitic gneisses from the Brimfield Schist. Following this, a kyanite zone overprint is evident from metasomatic kyanite-garnet-quartz-carbonate veins that cut across several lithologies within the Brimfield Schist, together with other regional occurrences of texturally late kyanite (Schumacher et al. 1989; Ague 1995; Thomson 2001).

Field relationships and geochronology document Acadian (~420–380 Ma) and Neoacadian (~360 Ma) metamorphism in the CMT (e.g. Rodgers 1981; Robinson and Tucker 1982; Schumacher et al. 1989; Armstrong et al. 1992; Getty and Gromet 1992; Wintsch et al. 1992, 2009; Robinson et al. 1998; Thomson 2001; Massey et al. 2017). Both of these events are recognized in metamorphic zircon from the Brimfield Schist and Bigelow Brook Formation, with the Neoacadian signal being dominant (Axler and Ague 2015c; Axler, unpublished PhD thesis). Rodgers (1981) suggested that the southern CMT originated in an accretionary prism formed during westward subduction before the Acadian collision, but this interpretation is not universally accepted (Robinson and Tucker 1982).

Elsewhere in the eastern United States, silica-undersaturated metapelitic or metagranitic rocks are found only in a handful of localities, including the Ordovician Cortlandt Complex (e.g. Rogers 1911; Barker 1964; Dorfler et al. 2014; Dorfler et al. 2015), the Silurian Cadillac Mountain granite (Nichols and Wiebe 1998), and the Siluro-Devonian Calderwood Neck Pendant in the Vinalhaven Pluton (Porter et al. 1999).

This is a preprint, the final version is subject to change, of the American Mineralogist (MSA)
Cite as Authors (Year) Title. American Mineralogist, in press.
DOI: https://doi.org/10.2138/am-2018-6543

ANALYTICAL METHODS

Quantitative mineral chemistry and backscattered electron (BSE) images were collected with a JEOL JXA-8530F field emission gun electron probe microanalyzer (EPMA) in the Yale University Department of Geology & Geophysics. Wavelength dispersive spectroscopy (WDS) was used for all mineral chemistry and elemental maps; quantitative analyses employed natural and synthetic standards and off-peak background corrections. Operating conditions were 15 kV accelerating voltage and 10.8 mm working distance with a focused beam. Beam current was 10 nA for biotite and feldspars, 20 nA for oxides, and 50 nA for garnet. Element mapping used a beam current of 20 nA and a dwell time of 100 ms for corundum, 200 nA and 100 ms for lower-resolution garnet maps and the spinel map, and 300 nA and 200 ms for the high-resolution garnet phosphorus map. Spinel host and oxide lamellae were reintegrated using an evenly spaced grid of 24 unfocused (25 μm) beam spots.

Ternary feldspar compositions for leucosome and matrix antiperthites were reconstructed following Ague et al. (2013). Compositions of host and lamellae were measured via EPMA, and (BSE) images of each grain were captured. Proportions of host and lamellae were determined by analyzing the BSE images in ImageJ (USA National Institutes of Health, imagej.nih.gov/ij/, accessed Aug 15, 2017). Precursor compositions were then calculated from EPMA data using host and lamellae proportions, assuming a representative cross-section. In the rare case that an antiperthite grain rim lacked lamellae, the rim was excluded from the calculation. Perthites were reintegrated using two techniques. The conservative reintegration counted only preserved lamellae in perthite hosts, and used evenly spaced grids of unfocused (25 μm) beam spots (Table 8). Image processing was not used for this group because they have irregularly distributed lamellae on several scales, from micrometers to sub-micrometers wide, as well as low BSE

This is a preprint, the final version is subject to change, of the American Mineralogist (MSA)
Cite as Authors (Year) Title. American Mineralogist, in press.
DOI: https://doi.org/10.2138/am-2018-6543

contrast between K-feldspar host and lamellae which complicates image processing. A test case for two-feldspar thermometry counted grain boundary plagioclase as well as lamellae for a well-preserved example (Fig. 7d, Table 9), and used spot analyses of host and lamellae combined with image analysis. Ternary feldspar temperature estimates were calculated using Theriak/Domino version 3.1 (De Capitani and Petrakakis 2010) with the feldspar activity models of Benisek et al. (2004), and Benisek et al. (2010). Two-feldspar thermometry for antiperthite–perthite+reintegrated grain boundary plagioclase used the method of Benisek et al. (2010), after Kroll et al. (1993).

Bulk rock chemistry (Table 1) was measured via X-ray fluorescence (XRF) of representative samples (150A/268A/269A) by SGS (see Ague 2011 and references therein for analytical details). Measured CaO was reduced assuming all P_2O_5 is hosted in apatite and LOI (taken to be H_2O) was re-calculated from the raw data based on a fixed Fe^{3+}/Fe(total) molar ratio. This ratio was deduced for each sample by comparing measured ilmenite compositions to those predicted by phase equilibrium calculations for a given Fe^{3+}/Fe(total) molar ratio (see Results section). Assuming ilmenite equilibration between the peak metamorphic conditions estimated herein and later lower granulite facies conditions along the *P-T* path of the Brimfield Schist (Ague et al. 2013) gives a Fe^{3+}/Fe(total) molar ratio of 1%. The phase relations are relatively insensitive to the Fe^{3+}/Fe^{2+}(total) ratio; values up to ~10% have no significant effect on the *P-T* estimates.

Pseudosection modeling used Theriak/Domino ver. 4.02 (De Capitani and Petrakakis, 2010) and the thermodynamic data file of D.K. Tinkham (version 02, http://dtinkham.net/peq.html#theriak-domino-files-holland-powell-2011-database, August 24, 2015) which contains the internally consistent tc-ds62 thermodynamic database of Holland and

This is a preprint, the final version is subject to change, of the American Mineralogist (MSA)
Cite as Authors (Year) Title. American Mineralogist, in press.
DOI: https://doi.org/10.2138/am-2018-6543

Powell (2011; referred to herein as HP11) and compatible activity models. The following activity models were used: Melt: (White et al. 2014a); Ternary feldspar: (Holland and Powell 2003); Garnet: (White et al. 2014a,b); White mica: (White et al 2014a); Biotite: (White et al. 2014a,b); Orthopyroxene: (White et al. 2014a,b); Sapphirine: (Wheller and Powell 2014); Cordierite: (White et al. 2014a,b); Spinel: (White et al. 2002); Ilmenite: (White et al. 2014b). The clinopyroxene model of Holland and Powell (1996) was used for simplicity and, thus, clinopyroxene phase relations should be regarded with caution. This has no impact on our conclusions as the *P-T* conditions recorded by the rocks are well outside the stability field of clinopyroxene. Importantly, HP11 is applicable to HPG conditions (White et al. 2014a).

RESULTS

Rock Description and Field Relations

The dominant mineral assemblage is garnet + spinel + corundum + plagioclase + K-feldspar + biotite + ilmenite, with leucosomes of two feldspars ± biotite surrounding garnet in some cases. The rock crops out as a single, uneven horizon several meters thick bounded by more siliceous, quartz-bearing gneisses. A fault marks the lower contact with the silicic gneiss. The upper contact, with a dark grey gneiss, is obscured by meter-scale leucosomes. Sheared leucosomes document thrust motion with a transport direction toward the modern E-SE (Fig. 2a).

The rocks vary from coarsely foliated to massive (Fig. 3a,e). Two textural styles are recognized: Type I is a "salt-and-pepper" variety where alkali feldspar is evenly distributed throughout the matrix, and Type II has uneven alkali feldspar distribution with coarse and interconnected leucosomes often defining a foliation (Fig. 3a). Leucosomes in Type I samples commonly have disaggregated edges. Both types contain the same mineral assemblage, although

This is a preprint, the final version is subject to change, of the American Mineralogist (MSA)
Cite as Authors (Year) Title. American Mineralogist, in press.
DOI: https://doi.org/10.2138/am-2018-6543

Type II contains the coarsest garnet, spinel, and corundum. In Type II samples, fine-grained bands several mm thick with numerous idiomorphic garnets and extremely fine-grained biotite suggest localized shearing; in some of these regions garnet porphyroblasts show trails and crusts of idiomorphic garnets in thin section (Fig. 4a). Most Type II samples contain trace pyrrhotite, chalcopyrite, and other sulfides in the matrix and as inclusions in corundum.

The chemical characteristics of the rocks likely reflect those of the protolith (e.g. some type of aluminous sediment or volcaniclastic deposit) modified by melt loss leading to silica undersaturation (e.g. Clifford et al. 1975; Lal et al. 1978; Grant 1985a,b) prior to the HPG stage. Protolith identification must await further geochemical study.

Mineral Descriptions and Chemistry

Garnet

Garnet is found mainly as isolated crystals and has sharp contacts with spinel and/or corundum with no intervening coronas or reaction zones (Figs. 3d and 4b). Megacrystic (up to ~10 cm) garnets occur within a sheared portion of the unit (Fig. 2b). In some samples, small (~100–300 μm) subhedral to euhedral garnets are present in addition to larger porphyroblasts (Fig. 4a). Garnet interiors commonly include grains of embayed spinel (Fig. 4b, 5a), former ternary feldspar (now with exsolution features), apatite, biotite, ilmenite, and, very rarely, sillimanite. Some garnet rims contain sillimanite, corundum, biotite, and spinel inclusions. Some garnets are partially altered to chlorite along cracks and rims, but are otherwise fresh. Garnets rimmed by leucosomes are inferred to be peritectic; these include the megacrystic variety in Figure 2b. Some peritectic garnet rims include antiperthites (Fig. 7a).

This is a preprint, the final version is subject to change, of the American Mineralogist (MSA)
Cite as Authors (Year) Title. American Mineralogist, in press.
DOI: https://doi.org/10.2138/am-2018-6543

Representative garnet compositions are given in Table 2. Garnet is almandine rich and often shows Mn depletion in rims (Table 2) as well as Mg depletion near contacts with biotite and along infilled cracks (Fig. 6c). Overall, garnets preserve little core-to-rim variation in Fe, Mg, and Ca. Where zonation of these elements is preserved, it is smooth, almost certainly reflecting diffusional relaxation (Fig. 6b-d).

Notably, some garnets have distinctly elevated phosphorus contents. In particular, the core of garnet in sample 294A-1 contains 0.18 wt% P_2O_5 (Table 2). Moreover, this garnet preserves a detailed textural record of modifications to zonation. The element map reveals that phosphorus is complexly and irregularly zoned in the garnet core, but a more regular core-to-rim zonation pattern is preserved in the bottom-left quadrant (Fig. 6b). The highest-phosphorus area has a sharp and irregular contact with the low-phosphorus area, showing lobate and irregular zoning comparable to that produced by interface-coupled dissolution-reprecipitation (ICDR) in garnets from UHP and HP granulites (Ague and Axler 2016). The ICDR process requires the interaction of fluids (defined broadly to also include melts) with minerals (e.g. Putnis and Austrheim 2010; Putnis and John 2010; Harlov et al. 2011). Thus, the isolated zones of phosphorus-rich garnet are likely relics of incomplete reactions with infiltrating fluid. A faint core-to-rim zoning of phosphorus is preserved in the bottom-right quadrant of the high-phosphorus region (Fig. 6b), suggesting that this is the original growth zoning and the low-phosphorus zones have been leached.

The core of the high-phosphorus garnet in sample 294A-1 contains oriented lamellae of rutile, ilmenite, and apatite. The lamellae are restricted to the P-rich portion of the garnet and are absent from immediately adjacent areas with lower phosphorus contents. They are oriented in 4 major directions and several subsidiary directions; the 4 major directions correspond to the

This is a preprint, the final version is subject to change, of the American Mineralogist (MSA)
Cite as Authors (Year) Title. American Mineralogist, in press.
DOI: https://doi.org/10.2138/am-2018-6543

<111> axes of the garnet host (e.g. Griffin et al. 1971; Axler and Ague 2015a). Some lamellae are composites of two minerals. Pairs of ilmenite with either apatite or rutile are present and show a range of morphologies (Fig. 4d).

Oriented rutile and ilmenite lamellae have been previously documented in garnet cores from the silica-saturated rocks in both the Brimfield Schist and the Bigelow Brook Formation (Ague and Eckert 2012; Ague et al. 2013; Axler and Ague 2015a). Depletion halos of Ti around these lamellae confirm an exsolution (precipitation) origin (Ague and Eckert 2012). For the silica-undersaturated lithology of this study, the restriction of lamellae to portions of garnet apparently unmodified by ICDR, their consistent lamellar habits, and their orientation along garnet zone axes, lead us to the interpretation that the inclusions exsolved from a precursor garnet richer in Ti and phosphorus; verification of this must await future crystallographic study.

Spinel

Spinel is found as black-green ragged, net-like matrix grains (~500 μm – 3 mm) and remarkable elongated, polycrystalline masses that reach nearly 6 cm in length (Fig. 3a,c) with long axes aligned roughly parallel to foliation. The largest grains contain thin (≤1 μm) platelets of Fe-Ti oxide that are oriented in 4 directions and can have broadly trigonal cross-sections. Oriented lamellae are largely absent in the rims of spinel masses and were not observed in spinel crystals less than ~1mm wide. Within the large spinel masses, crystallographic domains on the order of several mm are distinguishable in hand sample by their different reflections of light, and in thin section by changes in orientation of oriented oxide platelets (Fig. 5e). Larger spinels typically host inclusion pockets ~50 μm to ~500 μm across containing ternary feldspar with exsolution features, homogeneous feldspar, corundum, and biotite. Isolated feldspar inclusions are widespread.

This is a preprint, the final version is subject to change, of the American Mineralogist (MSA)
Cite as Authors (Year) Title. American Mineralogist, in press.
DOI: https://doi.org/10.2138/am-2018-6543

Analyzed spinel is hercynite rich and usually Zn poor (≤0.5 wt%; Table 3). Spinel is notably Mg poor relative to many garnet-spinel-corundum-bearing rocks (e.g. Padovani and Tracy 1981; Sengupta et al. 1999; Dharmapriya et al. 2015), especially those containing sapphirine (e.g. Ouzegane et al. 2003). Matrix spinel generally has between 2 and 2.5 wt% MgO; spinels included in garnet have elevated MgO relative to those in the matrix (e.g. sample 268A-2; 4.5 wt%), even those in contact with garnet. Matrix spinel from sample 294A-1 has the highest Cr_2O_3 content (~4.5 wt%), and particularly low MgO content (2.0 wt%).

The oriented oxide lamellae are too thin for individual EPMA analysis, but a reintegrated spinel composition was estimated with regularly spaced spot analyses, yielding a bulk TiO_2 content of 0.1 wt% (Table 3). This analysis method may underestimate the proportions of elements preferentially sequestered in the lamellae based on lamellae orientations relative to the sectioned plane, although the beam spot (25 μm diameter) was significantly larger than lamella width, and lamellae have a regular distribution within the host. We consider it likely that the lamellae exsolved to reduce spinel Ti content during retrogression.

Corundum

Corundum is present in two forms: as ≤1 cm subhedral to euhedral pink, purple, and blue crystals generally in contact with or within leucosomes in Type II samples (Fig. 3b,d), and colorless, jagged matrix grains often rimming spinel in both Type I and Type II samples (Figs. 4a, 5c). Both varieties have polysynthetic twinning in thin section and fluoresce red under long-wave ultraviolet light, with pink and purple crystals (or zones within crystals) showing stronger fluorescence than blue or colorless ones. The largest sapphires have concentric color zoning in hand sample (Fig. 3d). Most corundum crystals are fresh, although some in leucosomes are coated with chlorite.

A Cr element map of a representative coarse pink corundum in contact with leucosome surrounding peritectic garnet (in a Type II sample) reveals euhedral concentric zoning suggesting growth in contact with a fluid, most likely silicate melt, which may have supplied the trace elements (Fe, Ti, Cr) responsible for coloration (Figs. 3b and 5d). The presence of large colored corundum crystals, which only occur in Type II samples, appears to be tied to the presence of coarse leucosome networks.

Colorless matrix corundum commonly includes biotite and spinel and has few impurities, with negligible SiO_2, Fe_2O_3, TiO_2, and Cr_2O_3 contents (Table 4). Impurities are slightly higher in coarse, colored sapphire, but the mole fraction of corundum is >0.99 for all investigated crystals.

Biotite

Biotite crystals are present in both the leucosomes and the matrix and range from several millimeters across to only ~20μm in shear bands in Type II samples. Biotite may include ilmenite and, more rarely, spinel, and is commonly included in garnet cores and rims. Representative biotite analyses are given in Table 5. Matrix biotite Mg# typically ranges from 0.35 to 0.43, in keeping with the Fe-rich bulk composition of the rock. Higher values may reflect retrograde Mg-Fe exchange with garnet. Biotite inclusions in the high-phosphorus garnet of sample 294A-1 preserve greatly elevated TiO_2 contents exceeding 6.5 wt%. Armoring by garnet may have prevented Ti loss from these biotite crystals such that they retain peak or near-peak Ti contents (see below).

Feldspar

This is a preprint, the final version is subject to change, of the American Mineralogist (MSA)
Cite as Authors (Year) Title. American Mineralogist, in press.
DOI: https://doi.org/10.2138/am-2018-6543

Plagioclase is found in leucosomes, small leucocratic pockets in the matrix, and as inclusions in garnet, spinel, and biotite. Isolated matrix plagioclase grains are absent. Antiperthite is widespread in leucosomes but homogenous plagioclase is also found, typically adjacent to K-feldspar. The leucosomes surrounding peritectic garnet contain the antiperthites with the coarsest exsolution lamellae (Figs. 3b and 7a). Lamellae of K-feldspar ~1 mm wide in the core of the antiperthite with the coarsest lamellae (JAQ278A-1_ap3) are themselves perthitic and contain plagioclase lamellae up to ~2 μm across (Fig. 7e,f). Antiperthite host and lamellae compositions of coarse, unaltered grains in leucosomes, primarily surrounding garnet, are given in Tables 6 and 7.

Perthitic and homogeneous K-feldspar are found in leucosomes and as isolated matrix grains. K-feldspar crystals may contain inclusions of spinel and biotite. Some alkali feldspars show evidence of former elevated phosphorus content in the form of oriented apatite needles. These appear to be exsolved based on their sharp hexagonal cross-sections, consistent spatial distribution, and alignment along crystallographic planes (Fig. 7b). Alkali feldspar with elevated phosphorous content (up to 2.5 wt%) has been reported from pegmatites and granites (e.g. London et al. 1990; London 1992; Frýda and Breiter 1995; Kontak et al. 1996); usually alkali feldspar is significantly enriched in phosphorous compared to coexisting plagioclase feldspar, either as subsolvus separate grains or hypersolvus exsolved lamellae. In Ca-poor felsic rocks, alkali feldspars contain most of the bulk-rock phosphorous because apatite is scarce (London 1992). Reintegrated perthite compositions are given in Table 8.

Antiperthites can be relict from an igneous precursor (Štípská and Powell 2005). In this study, antiperthites in metamorphic leucosomes (commonly surrounding peritectic garnet and in contact with corundum) were judged to be metamorphic, and therefore preserving solvus

This is a preprint, the final version is subject to change, of the American Mineralogist (MSA)
Cite as Authors (Year) Title. American Mineralogist, in press.
DOI: https://doi.org/10.2138/am-2018-6543

350 temperatures representative of metamorphic conditions (e.g. Figs. 3b and 7a,e). The consistent
351 distribution of antiperthites with coarse exsolution lamellae and little retrogression or resorption
352 in leucosomes of different samples also indicates a metamorphic origin.

353 Perthites have several textures that indicate solid-state loss of plagioclase component.
354 Figure 7c illustrates a typical perthite with plagioclase lamellae in the core of the grain but not in
355 the rim. This suggests diffusional depletion of the plagioclase component into the matrix.
356 Plagioclase blebs have a tendency to pool along cracks and grain boundaries (Fig. 7d).
357 Plagioclase crystals adjacent to K-feldspar in leucosomes may represent lost plagioclase
358 component that has been recrystallized and consolidated. These characteristics suggest that the
359 perthites do not retain their peak plagioclase content, and thus do not record peak temperatures
360 for ternary feldspar reintegration thermometry. In contrast, antiperthites normally preserve
361 exsolution lamellae up to their edges (Fig. 7a). Our observation that antiperthites can preserve
362 exsolution lamellae near grain rims while perthites commonly do not has also been reported in
363 previous studies (e.g. Zulauf et al. 2002; Hokada and Suzuki 2006).

364 *Sillimanite*

365 Sillimanite is found most commonly as inclusions in garnet rims, and occasionally as
366 isolated matrix grains. Where foliation is present, sillimanite is aligned with biotite, the primary
367 matrix mineral defining the fabric, although a later generation of sillimanite cross-cuts the
368 foliation in some samples (Fig. 8). In a few examples, sillimanite inclusions in garnet cores form
369 trails that may record former foliation. These cores may be relict from prograde growth or may
370 have grown during retrogression.

371 *Ilmenite*

This is a preprint, the final version is subject to change, of the American Mineralogist (MSA)
Cite as Authors (Year) Title. American Mineralogist, in press.
DOI: https://doi.org/10.2138/am-2018-6543

Ilmenite is found as discrete, subhedral grains, and as isolated and netlike masses, usually in contact with spinel and corundum. Ilmenite does not deviate far from endmember composition, containing only minor impurities such as Si, Al, Mn, and Mg (Table 4); concentrations could have been higher, however, at peak thermal conditions. Ilmenites have low estimated Fe^{3+} contents and lack exsolution textures.

Ternary Feldspar Reintegration Thermometry

Antiperthites

The activity model of Benisek et al. (2010) returns the highest temperatures for reintegrated antiperthites, averaging 1053 °C ± 38 °C (2σ standard error) (Table 10; Fig. 9). The activity model of Benisek et al. (2004) yields a somewhat lower but still comparable mean of 1023 °C ± 20 °C (Table 10; Fig. 9). Both results use a pressure of 1.5 GPa, although the ternary feldspar solvi are only weakly pressure dependent. Regardless of activity model choice, antiperthites record T >1000 °C (mean ~1040 °C); as these are solvus T estimates, they are minima. These results are in agreement with those obtained for antiperthite and mesoperthite from silicic granulites in the Brimfield Schist and Bigelow Brook Formation (Ague et al. 2013; Axler and Ague 2015a), which gave solvus (minimum) temperatures ranging from ~900 °C–1000 °C. Zirconium-in-rutile thermometry likewise gives T in the 1000 °C range (Ague et al. 2013), with maximum estimates of nearly 1040 °C (Axler and Ague 2015a).

Perthites

Perthite T estimates have a significant dependence on activity model, and yield means of 868 °C ± 23 °C (Benisek et al. 2010) and 783 °C ± 44 °C (Benisek et al. 2004) (Table 10; Fig. 9; 2σ standard error). The two activity models differ regarding the behavior of the solvus for K-

This is a preprint, the final version is subject to change, of the American Mineralogist (MSA)
Cite as Authors (Year) Title. American Mineralogist, in press.
DOI: https://doi.org/10.2138/am-2018-6543

feldspar-rich ternary compositions (77–85 mol%) near the K-feldspar-albite join. The perthites have textures that clearly indicate loss of plagioclase component (Fig. 7 c,d), leading to *T* estimates that are erroneously low compared to those obtained from the antiperthites, regardless of activity model. To test this for thin section 278A-1, the perthite and coexisting grain boundary plagioclase in Figure 9d were reintegrated (Tables 9, 10) and the solvus *T* recomputed, yielding ~915 °C and ~1120 °C using Benisek et al. (2004) and (2010), respectively (Table 10). These estimates are more compatible with those obtained from antiperthites.

Furthermore, we tested the assumption that this reintegrated perthite was in equilibrium with reintegrated antiperthites in the same section (278A-1, Table 10) using two-feldspar thermometry and the method of Benisek et al. (2010) (after Kroll et al. 1993, which has been applied successfully to HPG rocks such as in O'Brien et al. 1997). This method is powerful in that it corrects for retrograde Na-K resetting and requires convergence of temperature estimates for all three feldspar endmembers. Pairing the reintegrated perthite with each of the three reintegrated antiperthites in 278A-1 (Table 10) gives temperatures of 1059°C, 1057 °C, and a non-converging, but still reasonably constrained, estimate of 1073 °C (Ab and An) to 1081 °C (Or) (Table 10). These estimates agree very well with the antiperthite results discussed above.

On this basis, we conclude that antiperthites and perthites were formerly in equilibrium before retrogression. Antiperthites mostly retained their exsolution products and, as a consequence, their reintegrated compositions yield reliable HPG solvus temperature estimates. Perthites, on the other hand, lost plagioclase component to grain boundaries and cracks. However, perthite reintegration that accounts for this lost plagioclase yields two-feldspar temperatures that are fully consistent with those from antiperthites alone.

Ti-in-biotite thermometry

This is a preprint, the final version is subject to change, of the American Mineralogist (MSA)
Cite as Authors (Year) Title. American Mineralogist, in press.
DOI: https://doi.org/10.2138/am-2018-6543

We employed the Ti-in-biotite thermometer of Wu and Chen (2015) and compared its results to ternary feldspar reintegration thermometry. We used the biotite with the highest measured Ti content, which is an inclusion in the high-phosphorus garnet of sample 294A-1 (Table 5). This biotite was likely shielded from retrogression by the surrounding garnet, so as to preserve high Ti concentrations from peak thermal conditions. The thermometer gives a temperature of ~1100 °C for the average pressure of 1.8 GPa obtained from the pseudosections described below. At 1.5 GPa, the result is ~1050 °C. Although the thermometer is only calibrated for T <840 °C, the estimates it returns agree well with the average obtained from ternary feldspar reintegration and two-feldspar thermometry.

Pseudosection Modeling

General Comments

Pressure is estimated based on the phase relations for the solid phase assemblage observed in the rocks: garnet + spinel + corundum + biotite + K-feldspar + ilmenite (the "full assemblage"). The phase field, which includes coexisting melt, is relatively narrow and is consistently positioned across bulk composition space, facilitating pressure estimation given constraints on temperature (Fig. 10). The field is also remarkably stable and occupies the same general position in pseudosections constructed for all three representative bulk compositions from Type I and Type II rocks. Despite differences in bulk composition among the samples, including SiO_2, Al_2O_3, K_2O, and FeO contents, the stability of this particular assemblage is insensitive to moderate changes in composition.

Pressure Estimation

The pseudosections for samples 150A, 268A, and 269A predict equilibration at 1.65–2.1 GPa, 1.6–2.1 GPa, and 1.7–2.05 GPa, respectively, for the average reintegrated antiperthite $T \pm$

This is a preprint, the final version is subject to change, of the American Mineralogist (MSA)
Cite as Authors (Year) Title. American Mineralogist, in press.
DOI: https://doi.org/10.2138/am-2018-6543

2σ standard error (Fig. 10). Simultaneous spinel breakdown and corundum growth (Fig. 5c) are predicted only within the full assemblage phase field (and its lower-temperature two-feldspar extension in 150A and 269A). This texture implies that the observed assemblage formed during cooling through the full assemblage field. Ternary plagioclase is absent from this field for each sample, but this is to be expected as it is only present in leucosomes, which were intentionally excluded from bulk analyses to ensure an accurate bulk composition determination for the matrix assemblage (e.g. Guevara and Caddick 2016). For samples 150A and 269A, the down-*T*, down-*P* granulite facies two-feldspar extension of the full assemblage field predicts albite-rich plagioclase rather than significantly ternary feldspar and, thus, does not represent the observed mineralogy.

Discussion of Pseudosection Results

Charge balance calculations indicate Fe^{3+} in spinel, ilmenite, and garnet (Tables 2–4). Ferric iron content estimation using ilmenite chemistry may underestimate the Fe^{3+}/Fe^{2+} ratio of the bulk rock if ilmenites equilibrated in the amphibolite facies. This would not affect results significantly, as pseudosections made assuming higher Fe^{3+} content up to ~10% yield similar results. The main difference is the expansion of garnet + spinel + corundum + biotite + ilmenite + K-feldspar + melt stability for bulk compositions with more Fe^{3+}. Likewise, increasing water content does not affect the results. Increasing molar H_2O by 15% produces nearly identical phase fields. Spinel has low Cr and Zn contents (Table 3). These trace elements can therefore safely be excluded from the modeling system with negligible effect on the stability range of spinel (e.g. Powell and Sandiford 1998; Shulters and Bohlen 1989; Diener and Powell 2010). Garnet and spinel, which can preserve strong chemical growth zonation, show relatively little core-to-rim variation in major or trace elements (Tables 2-3). The impact of prograde zonation

This is a preprint, the final version is subject to change, of the American Mineralogist (MSA)
Cite as Authors (Year) Title. American Mineralogist, in press.
DOI: https://doi.org/10.2138/am-2018-6543

463 in these modally major minerals on the accuracy of the measured effective bulk composition is
464 therefore minimized.

465 In general, preservation of peak garnet compositions at ~1000 °C is unlikely because
466 intracrystalline diffusion will be rapid (e.g. Chakraborty and Ganguly 1992; Faryad and
467 Chakraborty 2005; Carlson 2006; Chu and Ague 2015). For example, the $2\sqrt{Dt}$ characteristic
468 diffusive length scale for Fe in garnet at 1000 °C is several mm in 10^6 yr using the diffusion
469 coefficient calibration of Chu and Ague (2015). A further complication is that isopleths of garnet
470 Mg# and grossular content are sub-parallel across much of the modeled phase space for each
471 sample. Moreover, ICDR has clearly affected some garnets (Fig. 6). Nonetheless, sample 150A
472 preserves a garnet core Mg# that intersects the ternary feldspar *T* estimate within the full
473 assemblage field, and is closely correlated with core grossular content. The latter places
474 minimum garnet core *T* equilibration at ~975 °C (Fig. 10). The analyzed garnet in sample 150A
475 contains no plagioclase inclusions and the rock overall has much less biotite than samples 268A
476 and 269A; these factors may have restricted retrograde Ca and Fe-Mg exchange.

477 Garnet rim Mg# is consistently lower than core Mg#. Rim Mg# and grossular isopleths
478 tend to cluster in the lower granulite facies, in some cases at lower *P* than modeled on the
479 pseudosections. Core Mg# and grossular isopleths for sample 268A intersect at ~825 °C and ~0.6
480 GPa, which broadly correlates with the granulite facies overprint identified by Ague et al. (2013;
481 700–800 ^{o}C, 0.5–0.6 GPa) (Fig. 10). We note in this regard that garnet rims include sillimanite
482 (Fig. 4b) and rare matrix sillimanite cross-cuts foliation. If the rock remained reactive, the
483 pseudosections predict some garnet (and sillimanite) growth during cooling through the granulite
484 facies in the event of even a slight pressure increase following a UHT phase (Ague et al. 2013),
485 which could account for these sillimanite textures. Sillimanite is stable for each bulk composition

This is a preprint, the final version is subject to change, of the American Mineralogist (MSA)
Cite as Authors (Year) Title. American Mineralogist, in press.
DOI: https://doi.org/10.2138/am-2018-6543

below ~800 °C and ~0.8 GPa. Thus, based on general isopleth trends as well as sillimanite relationships, we conclude that the granulite overprint likely affected the silica-undersaturated lithology as well.

For all three analyzed samples, pseudosections predict between 35 and 41 vol% melt at 1040 °C and 1.8 GPa. This would have decreased the strength of the rock substantially and helped facilitate the observed widespread ductile shear deformation (Fig. 2a).

Results obtained using the thermodynamic dataset of Holland and Powell (1998) and compatible activity models also yield HPG pressure estimates of 1.55 to 1.7 GPa at 1040 °C. The feldspar activity model of Holland and Powell (2003) (which produces results similar to the Holland and Powell 1992 model and is standard in the Holland and Powell 2011 dataset) yields reintegrated ternary feldspar temperatures >1150 °C. This places pressures as high or even higher than our preferred results (Fig. 10).

DISCUSSION

Spinel Masses

The remarkable polycrystalline spinel masses documented herein deserve further comment, especially as they deviate strongly from the expected isometric spinel habit (Fig. 3c). The separation of each mass into crystallographic domains suggests that either a single cubic precursor grain underwent dynamic recrystallization, or that the grains are pseudomorphs or paramorphs after some other phase, perhaps with markedly different symmetry. As no high-pressure polymorphs of hercynitic spinel are known, we suggest that strain is responsible for recrystallizing formerly cubic spinel into an elongated, non-isometric form. Exsolution of Fe-Ti oxide could have occurred either before or after recrystallization, as each domain retained cubic

This is a preprint, the final version is subject to change, of the American Mineralogist (MSA)
Cite as Authors (Year) Title. American Mineralogist, in press.
DOI: https://doi.org/10.2138/am-2018-6543

symmetry (Fig. 5e). To the best of our knowledge, such large, elongated, and polycrystalline spinel forms are previously undescribed in metamorphic rocks.

The oriented Fe-Ti oxide lamellae in spinel are likely ilmenite, because they contain higher Ti than the host spinel, comparable Fe, and negligible Al. Intergrowths of spinel and ilmenite have been reported from UHT granulites (e.g. Sengupta et al. 1999) although they are not oriented lamellae of one phase inside of another. Nonetheless, these features have been interpreted as resulting from the expulsion of an ülvospinel (Fe_2TiO_4) component from a precursor high-Ti spinel (Sengupta et al. 1999). Given this, and the clear crystallographic shape preferred orientation of the lamellae, we suggest that they formed via exsolution and, thus, the Ti necessary to form the precipitates was soluble in hercynitic spinel at HPG or UHT conditions. This presupposes that the precursor phase was a spinel, but the isometric lattice constraints of the platelets suggest that they precipitated from a host phase with cubic symmetry, so spinel is the most likely candidate.

A reintegrated spinel formula shows that the precursor spinel contained 0.2 mol% ülvospinel component (277A-3; Table 3; computed following Sack and Ghiorso 1991a,b). An unexsolved spinel from a different sample (294A core; Table 3) has a higher ülvospinel mol% of 0.5. Other spinels in this sample show exsolution textures. Pseudosection calculations predict between 2 and 3 mol% ulvospinel component in spinel at peak conditions (1040 °C, 1.8 GPa) and ~2 mol% at UHT granulite facies conditions of 900 °C and 0.9 GPa, so the spinel precursors likely equilibrated with decreased Ti content during cooling from granulite facies conditions prior to ilmenite exsolution. The spinel textures deserve further work as they may hold information about pressure and temperature conditions, melt fraction, and strain rate or magnitude.

This is a preprint, the final version is subject to change, of the American Mineralogist (MSA)
Cite as Authors (Year) Title. American Mineralogist, in press.
DOI: https://doi.org/10.2138/am-2018-6543

Trace Elements and ICDR in Garnet

Rutile, ilmenite, and apatite lamellae in the core of the phosphorus-rich garnet of sample JAQ294A-1 are interpreted as precipitates from a garnet richer in Ti and phosphorus stable at $T \geq 1000$ °C and $P \geq \sim 1.8$ GPa. Similar textures are present in garnet cores from silicic granulites of the Brimfield Schist and Bigelow Brook Formation (Ague and Eckert 2012; Ague et al. 2013; Axler and Ague 2015a). Given that the silica-undersaturated HPG lithology and the silicic gneisses appear to share at least a retrograde history, we expect that the amount of Ti in the precursor garnet would have been stable at HPG or UHT conditions, similar to the conclusion of Ague and Eckert (2012). Solubility of Ti in garnet is thought to be controlled more by temperature than pressure at P <5 GPa, and although UHP majoritic substitutions may change this trend, the pressure dependence of Ti substitution in garnet is not yet clear (e.g. van Roermund et al. 2000; Zhang et al. 2003; Ackerson et al. 2017).

Apatite precipitates have been reported from garnets in UHP rocks and kimberlite xenoliths, and phosphorus-bearing garnets have been produced at UHP conditions in laboratory studies, demonstrating that phosphorus is soluble in garnet at high pressure (Fung and Haggerty 1995; Ye et al. 2000; Mposkos and Kostopoulos 2001; Hermann and Spandler 2008; Perchuck 2008; Konzett and Frost 2009; Konzett et al. 2012; Ruiz-Cruz and Sanz de Galdeano 2013; Alifirova et al. 2015; Axler and Ague 2015b; Sakamaki et al. 2016). Garnet in the diamondiferous Saidenbachite of the Erzgebirge contains >0.3 wt% P_2O_5, and garnet in the HPG Saxony granulite has nearly 0.5 wt% (Axler and Ague 2015b; Ague and Axler 2016). Indeed, high P_2O_5 in garnet (0.18 to 0.22 wt%) has been used to argue for prior UHP conditions in the Acadian orogen (Snoeyenbos and Koziol 2008; Peterman et al. 2016). Experiments by Konzett (2016) on basaltic eclogites demonstrate that garnet can hold 0.17 wt% P_2O_5 at 2 GPa and 975

This is a preprint, the final version is subject to change, of the American Mineralogist (MSA)
Cite as Authors (Year) Title. American Mineralogist, in press.
DOI: https://doi.org/10.2138/am-2018-6543

554 °C, comparable to the highest phosphorus content we have measured (0.18 wt% P_2O_5; Table 2).
555 Thus, although UHP conditions may not be required to produce the phosphorus levels we
556 observe, the Konzett (2016) experiments strongly suggest that the *P-T* conditions recorded by the
557 silica-undersaturated rocks are nonetheless unusual for crustal metamorphism.

558 The striking ICDR record preserved by irregular phosphorus zoning in garnet (Fig. 6a)
559 has many parallels to that found in garnet from the HPG Saxony Granulite (Ague and Axler
560 2016). In both samples, phosphorus zonation is highly irregular and shows little diffusional
561 smoothing. In the CT HPG sample, "cut-out" depletion halos around K-feldspar inclusions
562 reveal that the inclusion-host interface may provide an expedited fluid pathway, enabling ICDR
563 reactions to penetrate more efficiently in more poikiloblastic grains. Partial diffusional
564 smoothing of Ca and total smoothing of Mg provide further evidence that P diffuses more slowly
565 than major elements in garnet, making it a valuable recorder of growth zonation and later
566 modifications (e.g. Ague and Axler 2016). Fluid infiltration at HPG, granulite, or amphibolite-
567 facies conditions could have produced the observed ICDR zonation. Further research is required
568 to understand the extent to which ICDR may be responsible for modifying mineral compositions
569 in high-grade rocks, especially how to distinguish fluid signatures from melt signatures.

570 **Petrogenesis**

571 Thermometry and pseudosection modeling place equilibration of the silica-undersaturated
572 HPG lithology in the HPG realm at ~1040 °C and ~1.8 GPa. This pressure requires exhumation
573 from a depth of ~60 km (assuming lithostatic pressure) and thus either burial to the base of
574 orogenically thickened continental crust or thermal equilibration during exhumation from a hot
575 subduction zone. Both of these scenarios have been proposed for high-pressure granulites
576 (O'Brien and Rötzler 2003; O'Brien 2008). Eclogite facies rocks are thought to become high-

This is a preprint, the final version is subject to change, of the American Mineralogist (MSA)
Cite as Authors (Year) Title. American Mineralogist, in press.
DOI: https://doi.org/10.2138/am-2018-6543

pressure granulites during exhumation in some cases (e.g. Willner et al. 1997; Yao et al. 2000; Zhao et al. 2001; O'Brien and Rötzler 2003; Kim et al. 2006; Nahodilová et al. 2011). Marschall et al. (2003) suggested that Variscan granulites from the Schwarzwald were heated by basaltic magmas at the base of the orogenic belt and subsequently exhumed by orogenic extension. High levels of mantle heat input have also been invoked to explain high-*T* Variscan metamorphism (Sorger et al. 2018). Another possible parallel is the Gruf Complex of the Alps, which may have been heated to its UHT conditions by mantle diapirs (e.g. Galli et al. 2011). We conclude that the presence of HPG rocks in the CMT imposes new constraints on metamorphism and tectonism, namely that the thrust sheets of the southern CMT must have sampled the orogenic root and/or deeper settings during the assembly of composite Laurentia.

If the rocks formed in a subduction environment, their provenance is a hint that Acadian-Neoacadian terranes may hold similarly deeply subducted rocks to those known from contiguous Caledonian terranes in Greenland and Europe, which contain HPGs as well as the second-largest UHP terrane (by geographic extent) (Gilotti and Elvevold 2002; Gilotti and Krogh Ravna 2002; Hacker et al. 2010; Gilotti 2013; Klonowska et al. 2017). Some Acadian rocks have already been suggested as being indicative of deep subduction (e.g. Peterman et al. 2016).

IMPLICATIONS FOR SYENITES AND ALUMINOUS XENOLITHS

The partial melting which produced leucosomes has implications for both syenite genesis and the origins of highly aluminous xenoliths.

Leucosomes in the silica-undersaturated rocks, which were likely generated in situ, are effectively syenites consisting of two feldspars and biotite. Notably, syenite bodies with younger

This is a preprint, the final version is subject to change, of the American Mineralogist (MSA)
Cite as Authors (Year) Title. American Mineralogist, in press.
DOI: https://doi.org/10.2138/am-2018-6543

599 crystallization ages than peak metamorphic conditions are reported from several UHT terranes
600 (e.g. Brandt et al. 2003; Karmakar and Schenk 2016) and some UHT localities have syenitic
601 leucosomes (e.g. Hokada and Harley 2004). Moreover, lower-crustal UHT and HPG metapelites
602 have been explicitly considered as syenite producers (e.g. Litvinovsky et al. 2000; Tchameni et
603 al. 2001; Litvinovsky et al. 2002; Hacker et al. 2005; Shaffer et al. 2017). Nonetheless, the
604 prevailing consensus is that some mantle input is responsible for many syenite provinces (e.g.
605 Harris et al. 1983; Bailey 1987; Kramm and Kogarko 1994; Litvinovsky et al. 2002; Markl et al.
606 2010) and some syenite bodies have strong petrological evidence for mantle melt participation
607 (e.g. Lang et al. 1995), such as zoned syenite-pyroxenite dikes. Laboratory results showing that
608 syenites can be produced by HPG silicic rocks offer compelling evidence that high-grade
609 aluminous rocks like the silica-undersaturated rocks of this study may also produce syenites
610 (Litvinovsky et al. 2000).

611 The density of the CT silica-undersaturated HPGs may provide a key clue to an aspect of
612 syenite genesis and possibly also delamination. Delamination of the lower crust or lithospheric
613 mantle has been the focus of much previous work (e.g. Bird 1978; Bird 1979; Houseman et al.
614 1981; Rudnick 1995; Zegers and van Keken 2001; Anderson 2005) and delamination has been
615 suggested to follow alkaline igneous melt generation in lower crustal domains (Smithies and
616 Champion 1999). We suggest that the rocks of this study may be a syenite source that did not
617 melt to its full extent and delaminate.

618 Densities of the samples were calculated using Theriak-Domino (Table 1). At 1040 °C
619 and 1.8 GPa their average density is 3.0 g/cm^3, which is roughly as dense as basalt and
620 significantly denser than molten basalt (Ahrens and Johnson 1995). If 50% of the melt
621 calculated to be present at these *P-T* conditions was extracted from the rock, density would

This is a preprint, the final version is subject to change, of the American Mineralogist (MSA)
Cite as Authors (Year) Title. American Mineralogist, in press.
DOI: https://doi.org/10.2138/am-2018-6543

622 increase to 3.0–3.2 g/cm^3, which is near that of peridotitic or dunitic mantle (Daly et al. 1966;
623 Boyd et al. 1976; Rudnick 1995). If all of the melt was extracted (with no more being generated)
624 densities would reach 3.2 – 3.5 g/cm^3, roughly as dense as eclogite, which is negatively buoyant
625 relative to aesthenospheric mantle (Ahrens and Johnson 1995; Rudnick 1995; Zegers and van
626 Keken 2001). If more melting and melt loss occurred beyond what the CT rocks underwent,
627 density would be driven even higher as more feldspar and biotite are lost.

628 Depending on the mantle rock type directly beneath the base of orogenic crust, and the
629 degree to which that part of the mantle wedge was hydrated, delamination might release the
630 aluminous rock into the mantle (e.g. Hacker et al. 2011). Delamination could be triggered by
631 buoyant upwelling of magma pooling at the base of the crust, or crustal flow in response to
632 orogenic deformation (e.g. Bird 1978; Houseman et al. 1981). If delamination followed melt
633 generation and loss, the syenite source region would founder into the mantle, leaving only the
634 released melt within the crust.

635 We recognize that there are likely many complex aspects to syenite generation, and that
636 no one model is likely to account for the varied settings in which syenites are found. Further
637 study of syenites in terranes with anatectic UHT/HPG metapelites may well reveal that these
638 magmas can be generated at the base of orogenically thickened crust or in rift zones. Rocks like
639 those of this study may satisfy the requirements of "missing" syenite source regions both
640 chemically and physically.

641 Melt removal also has implications for the origins of highly aluminous xenoliths in
642 kimberlites containing various combinations of garnet, spinel, and corundum (e.g. Nixon et al.
643 1978; Padovani and Tracy 1981; Exley et al. 1983; Mazzone and Haggerty 1989).
644 Pseudosections (Fig. 10) show that large degrees of partial melting and melt removal would

leave behind highly aluminous restites enriched in garnet + spinel ± corundum (+ ilmenite) which would bear strong mineralogical similarities to the kimberlite xenoliths. As discussed above, if the restites reside at the base of the crust and are dense enough, they could delaminate and founder into the mantle. They would then be available to become entrained in kimberlites. Alternatively, such residues might also form by extreme melt loss from metasediments in subducted slabs, prior to incorporation in kimberlites (e.g. Mazzone and Haggerty 1989). This melt loss would, in turn, release syenitic melts and associated fluids to arc magma source regions. Either scenario is broadly compatible with current hypotheses for HPG genesis at the base of orogenically-thickened crust or as a consequence of "hot" subduction zone activity (e.g. O'Brien and Rötzler 2003; Marschall et al. 2003; O'Brien 2008). Delamination or subduction would help to explain the relatively uncommon occurrence of these rocks in exhumed orogenic belts.

This is a preprint, the final version is subject to change, of the American Mineralogist (MSA)
Cite as Authors (Year) Title. American Mineralogist, in press.
DOI: https://doi.org/10.2138/am-2018-6543

ACKNOWLEDGMENTS

We thank E.M. Stewart, J.A. Axler, S. Fererro, D.M. Rye, M.T. Brandon, and J.B. Murphy for discussions, J.O. Eckert Jr. for his EPMA expertise, M. Caddick, J.A.D. Connolly, and D.K. Tinkham for help with the HP11 database, and S. Nicolescu and F. Phillips for photography assistance. We also thank B.R. Hacker and C. A. Hauzenberger for thorough and constructive reviews. Becker Construction Company graciously allowed access to the field area. Support from the National Science Foundation (EAR-0744154, EAR-1250269, and EAR-1753553) and Yale University is gratefully acknowledged.

665 REFERENCES

666 Ackerson, M.R., Watson, E.B., Tailby, N.D. and Spear, F.S. (2017) Experimental investigation
667 into the substitution mechanisms and solubility of Ti in garnet. American Mineralogist, 102,
668 158-172.

669 Ague, J.J. (1995) Deep crustal growth of quartz, kyanite and garnet into large-aperture, fluid-
670 filled fractures, north-eastern Connecticut, USA. Journal of Metamorphic Geology, 13, 299-
671 314.

672 Ague, J.J. (2011) Extreme channelization of fluid and the problem of element mobility during
673 Barrovian metamorphism. American Mineralogist, 96, 333-352.

674 Ague, J.J. and Axler, J.A. (2016) Interface coupled dissolution-reprecipitation in garnet from
675 subducted granulites and ultrahigh-pressure rocks revealed by phosphorous, sodium, and
676 titanium zonation. American Mineralogist, 101, 1696-1699.

677 Ague, J.J. and Eckert, J.O. Jr. (2012) Precipitation of rutile and ilmenite needles in garnet:
678 Implications for extreme metamorphic conditions in the Acadian Orogen, U.S.A. American
679 Mineralogist, 840-855.

680 Ague, J.J., Eckert, J.O. Jr., Chu, X., Baxter, E.F. and Chamberlain, C.P. (2013) Discovery of
681 ultrahigh-temperature metamorphism in the Acadian orogen, Connecticut, USA. Geology,
682 41, 271-274.

683 Ahrens, T.J. and Johnson, M.L. (1995) Shock Wave Data for Rocks. In T.J. Ahrens Ed., Rock
684 Physics & Phase Relations: A Handbook of Physical Constants pp. 35-44. American
685 Geophysical Union, Washington, D.C.

686 Aleinikoff, J. N., Wintsch, R. P., Tollo, R. P., Unruh, D. M., Fanning, C. M. & Schmitz, M. D.
687 (2007) Ages and origins of rocks of the Killingworth dome, south-central Connecticut:
688 implications for the tectonic evolution of southern New England. American Journal of
689 Science, 307, 63-118.

690 Alifirova, T.A., Pokhilenko, L.N. and Korsakov, A.V. (2015) Apatite, SiO_2, rutile and
691 orthopyroxene precipitates in minerals of eclogite xenoliths from Yakutian kimberlites,
692 Russia. Lithos, 226, 31-49.

693 Anderson, D.L. (2005) Large Igneous Provinces, Delamination, and Fertile Mantle. Elements, 1,
694 271-275.

695 Armstrong, T.R., Tracy, R.J. and Hames, W.E. (1992) Contrasting styles of Taconian, Eastern
696 Acadian and Western Acadian metamorphism, central and western New England. Journal of
697 Metamorphic Geology, 10, 415-426.

698 Asami, M., Grew, E.S. and Makimoto, H. (1990) A staurolite-bearing corundum-garnet gneiss
699 from the Eastern Sør Rondane Mountains, Antarctica. Proceedings of the National Institute
700 of Polar Research Symposium on Antarctic Geoscience, 4, 22-40.

701 Asami, M., Makimoto, H. and Grew, E.S. (1989) Geology of the Eastern Sør Rondane
702 Mountains, East Antarctica. Proceedings of the National Institute of Polar Research
703 Symposium on Antarctic Geoscience, 3, 81-99.

704 Axler, J.A. and Ague, J.J. (2015) Oriented multiphase needles in garnet from ultrahigh-
705 temperature granulites, Connecticut, U.S.A. American Mineralogist, 100, 2254-2271.

706 Axler, J.A. and Ague, J.J. (2015) Exsolution of rutile or apatite precipitates surrounding ruptured
707 inclusions in garnet from UHT and UHP rocks. Journal of Metamorphic Geology, 33, 829-
708 848.

709 Axler, J.A. and Ague, J.J (2015) Too hot for zircons? U-Pb zircon geochronology of the
710 ultrahigh-temperature (UHT) region of the Central Maine Terrane, Connecticut, USA.
711 Geological Society of America Abstracts with Programs, 47, 773.

712 Bailey, D.K. (1987) Mantle metasomatism - perspective and prospect. In J.G. Fitton and B.G.J.
713 Upton, Eds., Alkaline Igneous Rocks, Geological Society, London, Special Publications, 30,
714 1-13.

715 Baldwin, J.A., Bowring, S.A., and Williams, M.L. (2003) Petrological and geochronological
716 constraints on high pressure, high temperature metamorphism in the Snowbird tectonic zone,
717 Canada. Journal of Metamorphic Geology, 21, 81-98.

718 Barker, F. (1964) Reaction between mafic magmas and pelitic schist, Cortlandt, New York.
719 American Journal of Science, 262, 614-634.

720 Benisek, A., Dachs, E. and Kroll, H. (2010) A ternary feldspar-mixing model based on
721 calorimetric data: development and application. Contributions to Mineralogy and Petrology,
722 160, 327-337.

723 Benisek, A., Kroll, H. and Cemič, L. (2004) New developments in two-feldspar thermometry.
724 American Mineralogist, 89, 1496-1504.

725 Bird, P. (1978) Initiation of intracontinental subduction in the Himalaya. Journal of Geophysical
726 Research, 83, 4975-4987.

727 Bird, P. (1979) Continental Delamination and the Colorado Plateau. Journal of Geophysical
728 Research, 84, 7561-7571.

729 Boyd, F.R. and McCallister, R.H. (1976) Densities of fertile and sterile garnet peridotites.
730 Geophysical Research Letters, 3, 509-512.

731 Brandt, S., Klemd, R. and Okrusch, M. (2003) Ultrahigh-Temperature Metamorphism and
732 Multistage Evolution of Garnet-Orthopyroxene Granulites from the Proterozoic Epupa
733 Complex, NW Namibia. Journal of Petrology, 44, 1121-1144.

734 Brown, M. (2006) Duality of thermal regimes is the distinctive characteristic of plate tectonics
735 since the Neoarchean. Geology, 34, 961-964.

736 Carlson, W.D. (2006) Rates of Fe, Mg, Mn, and Ca diffusion in garnet. American Mineralogist,
737 91, 1-11.

738 Chakraborty, S. and Ganguly, J. (1992) Cation diffusion in aluminosilicate garnets: experimental
739 determination in spessartine-almandine diffusion couples, evaluation of effective binary
740 diffusion coefficients, and applications. Contribution to Mineralogy and Petrology, 111, 74-
741 86.

742 Chamberlain, C.P. and England, P.C. (1985) The Acadian Thermal History of the Merrimack
743 Synclinorium in New Hampshire. The Journal of Geology, 93, 593-602.

744 Chu, X. and Ague, J.J. (2015) Analysis of experimental data on divalent cation diffusion kinetics
745 in aluminosilicate garnets with application to timescales of peak Barrovian metamorphism,
746 Scotland. Contributions to Mineralogy and Petrology, 170:25.

747 Clifford, T.N., Stumpfl, E.F. and McIver, J.R. (1975) A sapphirine-cordierite-bronzite-
748 phlogopite paragenesis from Namaqualand, South Africa. Mineralogical Magazine, 40, 347-
749 356.

750 Daly, R.A., Manger, G.E. and Clark, S.P. Jr. (1966) Density of rocks. In S.P. Clark Jr. Ed.,
751 Handbook of Physical Constants – *Revised Edition*. Geological Society of America Memoir
752 97, 19-26.

753 De Capitani, C. and Petrakakis, K. (2010) The computation of equilibrium assemblage diagrams
754 with Theriak/Domino software. American Mineralogist, 95, 1006-1016.

755 Dharmapriya, P.L., Malaviarachchi, S.P.K., Galli, A., Su, B., Subasinghe, N.D. and Dissanayake,
756 C.B. (2015) Rare evidence for formation of garnet + corundum during isobaric cooling of

ultrahigh temperature metapelites: New insights for retrograde *P-T* trajectory of the Highland Complex, Sri Lanka. Lithos, 220-223, 300-317.

Diener, J.F.A. and Powell, R. (2010) Influence of ferric iron on the stability of mineral assemblages. Journal of Metamorphic Geology, 28, 599-613.

Dorfler, K.M., Tracy, R.J., and Caddick, M.J. (2014) Late-stage orogenic loading revealed by contact metamorphism in the northern Appalachians, New York. Journal of Metamorphic Geology, 32, 113-132.

Dorfler, K.M., Caddick, M.J., and Tracy, R.J. (2015) Thermodynamic Modeling of Crustal Melting Using Xenolith Analogs from the Cortlandt Complex, New York, USA. Journal of Petrology, 56, 389-408.

Exley, R.A., Smith, J.V. and Dawson, J.B. (1983) Alkremite, garnetite, and eclogite xenoliths from Bellsbank and Jagersfontein, South Africa. American Mineralogist, 68, 512-516.

Fahey, R.J. and Pease, M.H. Jr. (1977) Preliminary bedrock geologic map of the South Coventry quadrangle, Tolland County, Connecticut. U.S. Geological Survey Open-File Report, 77-587.

Faryad, S.W., and Chakraborty, S. (2005) Duration of Eo-Alpine metamorphic events obtained from multicomponent diffusion modeling of garnet: a case study from the Eastern Alps. Contributions to Mineralogy and Petrology, 150, 306-318.

Ferrero, S., Axler, J., Ague, J.J., Wunder, B. and Ziemann, M.A. (2017) Preserved anatectic melt in ultrahigh-temperature (or high pressure?) felsic granulites, Connecticut, US. Geophysical Research Abstracts, 19, EGU2017-9692-1.

777 Frýda, J. and Breiter, K. (1995) Alkali feldspars as a main phosphorus reservoirs in rare-metal
778 granites: three examples from the Bohemian Massif (Czech Republic). Terra Nova, 7, 315-
779 320.

780 Fung, A.T. and Haggerty, S.E. (1995) Petrography and mineral compositions of eclogites from
781 the Koidu Kimberlite Complex, Sierra Leone. Journal of Geophysical Research, 100, 20451-
782 20473.

783 Galli, A., Le Bayon, B., Schmidt, M.W., Burg, J-P., Caddick, M.J. and Reusser, E. (2011)
784 Granulites and charnockites of the Gruf Complex: Evidence for Permian ultra-high
785 temperature metamorphism in the Central Alps. Lithos, 124, 17-45.

786 Gilotti, J. (2013) The Realm of Ultrahigh-Pressure Metamorphism. Elements, 9, 255-260.

787 Gilotti, J.A. and Elvevold, S. (2002) Extensional exhumation of a high-pressure granulite terrane
788 in Payer Land, Greenland Caledonides: structural, petrologic, and geochronologic evidence
789 from metapelites. Canadian Journal of Earth Science, 39, 1169-1187.

790 Gilotti, J.A. and Krogh Ravna, E.J. (2002) First evidence for ultrahigh-pressure metamorphism
791 in the North-East Greenland Caledonides. Geology, 30, 551-554.

792 Getty, S.R., and Gromet, L.P. (1992) Geochronological constraints on ductile deformation,
793 crustal extension, and doming about a basement-cover boundary, New England
794 Appalachians. American Journal of Science, 292, 359-397, doi: 10.2475/ajs.292.6.359.

795 Grant, J.A. (1985) Phase equilibria in low-pressure partial melting of pelitic rocks. American
796 Journal of Science, 285, 409-435.

797 Grant, J.A. (1985) Phase equilibria in partial melting of pelitic rocks. In J.R. Ashworth Ed.,
798 Migmatites pp. 86-144. Chapman & Hall, New York, NY.

799 Griffin, W.L., Jensen, B.B. and Misra, S.N. (1971) Anomalously elongated rutile in eclogite-
800 facies pyroxene and garnet. Norsk Geologisk Tidsskrift, 51, 177-185.

801 Guevara, V. and Caddick, M. (2016) Shooting at a moving target: Phase equilibria modelling of
802 high-temperature metamorphism. Journal of Metamorphic Geology, 34, 209-235.

803 Hacker, B.R., Luffi, P., Lutkov, V., Minaev, V., Ratschbacher, L., Plank, T., Ducea, M., Patiño-
804 Douce, A., McWilliams, M., and Metcalf, J. (2005) Near-Ultrahigh Pressure Processing of
805 Continental Crust: Miocene Crustal Xenoliths from the Pamir. Journal of Petrology, 46,
806 1661-1687.

807 Hacker, B.R., Andersen, T.B., Johnston, S., Kylander-Clark, A.R.C., Peterman, E.M., Walsh,
808 E.O. and Young, D. (2010) High-temperature deformation during continental-margin
809 subduction & exhumation: The ultrahigh-pressure Western Gneiss Region of Norway.
810 Tectonophysics, 480, 149-171.

811 Hacker, B.R., Kelemen, P.B., and Behn, M.D. (2011) Differentiation of the continental crust by
812 relamination. Earth and Planetary Science Letters, 307, 501-516.

813 Harley, S.L. (1998) On the occurrence and characterization of ultrahigh-temperature crustal
814 metamorphism. In P.J. Treloar and P.J. O'Brien Eds., What Drives Metamorphism and
815 Metamorphic Reactions? Geological Society, London, Special Publications, 138, 81-107.

816 Harlov, D.E., Wirth, R. and Hetherington, C.J. (2011) Fluid-mediated partial alteration in
817 monazite: the role of coupled dissolution-reprecipitation in element redistribution and mass
818 transfer. Contributions to Mineralogy and Petrology, 162, 329-348.

819 Harris, N. (1981) The Application of Spinel-Bearing Metapelites to *P/T* Determinations: An
820 Example from South India. Contributions to Mineralogy and Petrology, 76, 229-233.

821 Harris, N.B.W., Duyverman, H.J. and Almond, D.C. (1983) The trace element and isotope
822 geochemistry of the Sabaloka Igneous Complex, Sudan. Journal of the Geological Society of
823 London, 140, 245-256.

824 Hermann, J. and Spandler, C.J. (2008) Sediment Melts at Sub-arc Depths: an Experimental
825 Study. Journal of Petrology, 49, 717-740.

826 Hibbard, J. P., van Staal, C. R., Rankin, D. R. & Williams, H. (2006) Lithotectonic map of the
827 Appalachian orogen, Canada-United States of America, scale 1:1,500,000. Geological
828 Survey of Canada.

829 Hokada, T. and Suzuki, S. (2006) Feldspar in felsic orthogneiss as indicator for UHT crustal
830 processes. Journal of Mineralogical and Petrological Sciences, 101, 260-264.

831 Hokada, T. and Harley, S. (2004) Zircon growth in UHT leucosome: constraints from zircon-
832 garnet rare earth elements (REE) relations in Napier Complex, East Antarctica. Journal of
833 Mineralogical and Petrological Sciences, 99, 180-190.

834 Holland, T. and Powell, R. (1996) Thermodynamics of order-disorder in minerals: II. Symmetric
835 formalism applied to solid solutions. American Mineralogist, 81, 1425-1437.

836 Holland, T.J.B. and Powell, R. (1998) An internally consistent thermodynamic data set for
837 phases of petrological interest. Journal of Metamorphic Geology, 16, 309-343.

838 Holland, T. and Powell, R. (2003) Activity-composition relations for phases in petrological
839 calculations: an asymmetric multicomponent formulation. Contributions to Mineralogy and
840 Petrology, 145, 492-501.

841 Holland, T.J.B. and Powell, R. (2011) An improved and extended internally consistent
842 thermodynamic dataset for phases of petrological interest, involving a new equation of state
843 for solids. Journal of Metamorphic Geology, 29, 333-383.

844 Houseman, G.A., McKenzie, D.P. and Molnar, P. (1981) Convective instability of a thickened
845 boundary layer and its relevance for the thermal evolution of continental convergent belts.
846 Journal of Geophysical Research, 86, 6115-6132.

847 Indares, A. (1993) Eclogitized gabbros from the eastern Grenville Province: Textures,
848 metamorphic context, and implications. Canadian Journal of Earth Sciences, 30, 159-173.

849 Indares, A. (1995) Metamorphic interpretation of high-pressure-temperature metapelites with
850 preserved growth zoning in garnet, eastern Grenville Province, Canadian Shield. Journal of
851 Metamorphic Geology, 13, 475-486.

852 Indares, A. (1997) Garnet-kyanite clinopyroxenites and garnet-kyanite restites from the
853 Manicouagan Imbricate Zone: a case of high-P – high-T metamorphism in the Grenville
854 Province. Canadian Mineralogist, 35, 1161-1171.

855 Indares, A., Dunning, G. (2001) Partial Melting of High-*P–T* Metapelites from the Tshenukutish
856 Terrane (Grenville Province): Petrography and U–Pb Geochronology. Journal of Petrology,
857 42, 1547-1565.

858 Indares, A., Dunning, G., Cox, R., Gale, D., Connelly, J. (1998) High-pressure, high-temperature
859 rocks from the base of thick continental crust: Geology and age constraints from the
860 Manicouagan Imbricate Zone, eastern Grenville Province. Tectonics, 17, 426-440.

861 Karmakar, S. and Schenk, V. (2016) Mesoproterozoic UHT metamorphism in the Southern
862 Irumide Belt, Chipata, Zambia: Petrology and in-situ monazite dating. Precambrian
863 Research, 275, 332-356.

864 Kelsey, D.E. (2008) On ultrahigh-temperature crustal metamorphism. Gondwana Research, 13,
865 1-29.

866 Kelsey, D.E., White, R.W. and Powell, R. (2005) Calculated phase equilibria in K_2O-FeO-MgO-
867 Al_2O_3-SiO_2-H_2O for silica-undersaturated sapphirine-bearing mineral assemblages. Journal
868 of Metamorphic Geology, 23, 217-239.

869 Kim, S.W., Oh, C.W., Williams, I.S., Rubatto, D., Ryu, I., Rajesh, V.J., Kim, C., Guo, J. and
870 Zhai, M. (2006) Phanerozoic high-pressure eclogite and intermediate-pressure granulite
871 facies metamorphism in the Gyeonggi Massif, South Korea: Implications for the eastward
872 extension of the Dabie-Sulu continental collision zone. Lithos, 92, 357-377.

873 Klonowska, I., Janák, M., Majka, J., Petrík, I., Froitzheim, N., Gee, D.G. and Sasinkova, V.
874 (2017) Microdiamond on Åreskutan confirms regional UHP metamorphism in the Seve

875 Nappe Complex of the Scandanavian Caledonides. Journal of Metamorphic Geology, 35,
876 541-564.

877 Kontak, D.J., Martin, R.F. and Richard, L. (1996) Patterns of phosphorus enrichment in alkali
878 feldspar, South Mountain Batholith, Nova Scotia, Canada. European Journal of Mineralogy,
879 8, 805-824.

880 Konzett, J. (2016) From phosphates to silicates and back: An experimental study on the transport
881 and storage of phosphorus in eclogites during uplift and exhumation. American Mineralogist,
882 101, 1756-1768.

883 Konzett, J. and Frost, D.J. (2009) The High *P*-*T* Stability of Hydroxyl-apatite in Natural and
884 Simplified MORB–an Experimental Study to 15 GPa with Implications for Transport and
885 Storage of Phosphorus and Halogens in Subduction Zones. Journal of Petrology, 50, 2043-
886 2062.

887 Konzett, J., Rhede, D. and Frost, D.J. (2012) The high PT stability of apatite and Cl partitioning
888 between apatite and hydrous potassic phases in peridotite: an experimental study to 19 GPa
889 with implications for the transport of P, Cl and K in the upper mantle. Contributions to
890 Mineralogy and Petrology, 163, 277-296.

891 Kotková, J. (2007) High-pressure granulites of the Bohemian Massif: recent advances and open
892 questions. Journal of Geosciences, 52, 45-71.

893 Kramm, U. and Kogarko, L.N. (1994) Nd and Sr isotope signatures of the Khibina and Lovozero
894 agpaitic centres, Kola Alkaline Province, Russia. Lithos, 32, 225-242.

895 Kroll, H., Evangelakakis, C. and Voll, G. (1993) Two-feldspar geothermometry: a review and
896 revision for slowly-cooled rocks. Contributions to Mineralogy and Petrology, 114, 510-518.

897 Lal, R.K., Ackermand, D., Seifert, F. and Haldar, S.K. (1978) Chemographic Relationships in
898 Sapphirine-Bearing Rocks From Sonapahar, Assam, India. Contributions to Mineralogy and
899 Petrology, 67, 169-187.

900 Lang, J.R., Lueck, B., Mortensen, J.K., Russell, J.K., Stanley, C.R. and Thompson, J.F.H. (1995)
901 Triassic-Jurassic silica-undersaturated and silica-saturated alkalic intrusions in the Cordillera
902 of British Columbia: Implications for arc magmatism. Geology, 23, 451-454.

903 Litvinovsky, B.A., Steele, I.M. and Wickham, S.M. (2000) Silicic Magma Formation in
904 Overthickened Crust: Melting of Charnockite and Leucogranite at 15, 20 and 25 kbar.
905 Journal of Petrology, 41, 717-737.

906 Litvinovsky, B.A., Jahn, B., Zanvilevich, A.N., Saunders, A., Poulain, S., Kuzmin, D.V.,
907 Reichow, M.K. and Titov, A.V. (2002) Petrogenesis of syenite–granite suites from the
908 Bryansky Complex (Transbaikalia, Russia): implications for the origin of A-type granitoid
909 magmas. Chemical Geology, 189, 105-133.

910 London, D., Černý, P., Loomis, J.L. and Pan, J.J. (1990) Phosphorus in Alkali Feldspars of Rare-
911 Element Granitic Pegmatites. Canadian Mineralogist, 28, 771-786.

912 London, D. (1992) Phosphorus in S-type magmas: The P_2O_5 content of feldspars from
913 peraluminous granites, pegmatites, and rhyolites. American Mineralogist, 77, 126-145.

914 Markl, G., Marks, M.A.W. and Frost, B.R. (2010) On the Controls of Oxygen Fugacity in the
915 Generation and Crystallization of Peralkaline Melts. Journal of Petrology, 51, 1831-1847.

916 Marschall, H.R., Kalt, A. and Hanel, M. (2003) *P–T* Evolution of a Variscan Lower-Crustal
917 Segment: a Study of Granulites from the Schwarzwald, Germany. Journal of Petrology, 44,
918 227-253.

919 Massey, M.A., Moecher, D.P., Walker, T.B., O'Brien, T.M. and Rohrer, L.P. (2017) The role
920 and extent of dextral transpression and lateral escape on the post-Acadian tectonic evolution
921 of south-central New England. American Journal of Science, 317, 34-94.

922 Mazzone, P. and Haggerty, S.E. (1989) Peraluminous xenoliths in kimberlite: Metamorphosed
923 restites produced by partial melting of pelites. Geochimica et Cosmochimica Acta, 53, 1551-
924 1561.

925 Mposkos, E.D. and Kostopoulos, D.K. (2001) Diamond, former coesite and supersilicic garnet in
926 metasedimentary rocks from the Greek Rhodope: a new ultrahigh-pressure metamorphic
927 province established. Earth and Planetary Science Letters, 192, 497-506.

928 Müller, T., Massonne, H.J., and Willner, A.P. (2015) Timescales of exhumation and cooling
929 inferred by kinetic modeling: An example using a lamellar garnet pyroxenite from the
930 Variscan Granulitgebirge, Germany. American Mineralogist, 100, 747-759.

931 Nahodilová, R., Faryad, S.W., Dolejš, D., Tropper, P. and Konzett, J. (2011) High-pressure
932 partial melting and melt loss in felsic granulites in the Kutná Hora complex, Bohemian
933 Massif (Czech Republic). Lithos, 125, 641-658.

934 Nasdala, L. and Massonne, H. (2000) Microdiamonds from the Saxonian Erzgebirge,
935 Germany: *in situ* micro-Raman characterization. European Journal of Mineralogy, 12, 495-
936 498.

937 Nichols, G.T. and Wiebe, R.A. (1998) Desilication veins in the Cadillac Mountain granite
938 (Maine, USA): a record of reversals in the SiO_2 solubility of H_2O-rich vapour released during
939 subsolidus cooling. Journal of Metamorphic Geology, 16, 795-808.

940 Nixon, P.H., Chapman, N.A. and Gurney, J.J. (1978) Pyrope-Spinel (Alkremite) Xenoliths From
941 Kimberlite. Contributions to Mineralogy and Petrology, 65, 341-346.

942 O'Brien, P.J., Kröner, A., Jaeckel, P., Hegner, E., Żelanźniewicz, A. and Kryza, R. (1997)
943 Petrological and Isotopic Studies on Palaeozoic High-pressure Granulites, Góry Sowie Mts,
944 Polish Sudetes. Journal of Petrology, 38, 433-456.

945 O'Brien, P.J. (2006) Type-locality granulites: high-pressure rocks formed at eclogite-facies
946 conditions. Mineralogy and Petrology, 86, 161-175.

947 O'Brien, P.J. (2008) Challenges in high-pressure granulite metamorphism in the era of
948 pseudosections: reaction textures, compositional zoning and tectonic interpretation with
949 examples from the Bohemian Massif. Journal of Metamorphic Geology, 26, 235-251.

950 O'Brien, P.J. and Rötzler, J. (2003) High-pressure granulites: formation, recovery of peak
951 conditions and implications for tectonics. Journal of Metamorphic Geology, 21, 3-20.

952 Osanai, Y., Sajeev, K., Owada, M., Wilbert Kehelpannala, K.V., Bernard Prame, W.K., Nakano,
953 N. and Jayatileke, S. (2006) Metamorphic evolution of high-pressure and ultrahigh-

954 temperature granulites from the Highland Complex, Sri Lanka. Journal of Asian Earth
955 Sciences, 28, 20-37.

956 Ouzegane, K., Guiraud, M. and Kienast, J.R. (2003) Prograde and Retrograde Evolution in High-
957 temperature Corundum Granulites (FMAS and KFMASH Systems) from In Ouzzal Terrane
958 (NW Hoggar, Algeria). Journal of Petrology, 44, 517-545.

959 Padovani, E.R. and Tracy, R.J. (1981) A pyrope-spinel (alkremite) xenolith from Moses Rock
960 Dike: first known North American occurrence. American Mineralogist, 66, 741-745.

961 Peper, J.D. and Pease, M.H. Jr. (1975) Geologic map of the Westford quadrangle, Connecticut.
962 U.S. Geological Survey Quadrangle Map, GQ-1214.

963 Perchuck, A.L. (2008) Unusual Inclusions in Garnet from the Diamond-Bearing Gneiss of the
964 Erzgebirge, Germany. Geochemistry International, 46, 296-303.

965 Peterman, E.M., Snoeyenbos, D.R., Jercinovic, M.J. and Kylander-Clark, A. (2016) Dissolution-
966 reprecipitation metasomatism and growth of zircon within phosphatic garnet in metapelites
967 from western Massachusetts. American Mineralogist, 101, 1792-1806.

968 Porter, B.S., Wiebe, R., Cheney, J.T. (1999) Regional and contact metamorphism of Paleozoic
969 greenschist and pelites, Vinalhaven Island, Maine. Geological Society of America Abstracts
970 with Programs, 31, A-61.

971 Powell, R. and Sandiford, M. (1988) Sapphirine and spinel phase relationships in the system
972 $FeO–MgO–Al_2O_3–SiO_2–TiO_2–O_2$ in the presence of quartz and hypersthene. Contributions to
973 Mineralogy and Petrology, 98, 64-71.

974 Putnis, A. and Austrheim, H. (2010) Fluid-induced processes: metasomatism and metamorphism.
975 Geofluids, 10, 254-269.

976 Putnis, A. and John, T. (2010) Replacement Processes in the Earth's Crust. Elements, 6, 159-
977 164.

978 Robinson, P. (1978) The Bronson Hill anticlinorium and Merrimack synclinorium in central
979 Massachusetts – an Acadian "Pennine zone." Geological Society of America Abstracts with
980 Programs, 10, 82.

981 Robinson, P. and Tucker, R.D. (1982) The Merrimack Synclinorium in Northeastern
982 Connecticut. American Journal of Science, 282, 1735-1744.

983 Robinson, P., Tucker, R.D., Bradley, D., Berry, H.N., IV and Osberg, P.H. (1998) Paleozoic
984 orogens in New England, USA. GFF, Vol. 120 (Pt. 2, June), pp. 119-148. Stockholm. ISSN
985 1103-5897.

986 Rodgers, J. (1981) The Merrimack Synclinorium in Northeastern Connecticut. American Journal
987 of Science, 281, 176-186.

988 Rodgers, J. (1985) Bedrock Geological Map of Connecticut, scale 1:125,000. Connecticut
989 Geological and Natural History Survey, Department of Environmental Protection,
990 Hartford, Connecticut.

991 Rogers, G.S. (1911) Geology of the Cortlandt Series and its emery deposits. New York
992 Academy of Science Annals, 21, 11-86.

993 Rötzler, J. (1992) The petrogenesis of pyroxene-free granulites and metapelites of the Saxonian
994 granulite massif, Germany. Geotektonische Forschungen 77, 1-100 (in German).

995 Rötzler, J. and Romer, R.L. (2001) *P-T-t* Evolution of Ultrahigh-Temperature Granulites from
996 the Saxon Granulite Massif, Germany. Part I: Petrology. Journal of Petrology, 42, 1995-
997 2013.

998 Rudnick, R.L. (1995) Making continental crust. Nature, 378, 571-578.

999 Ruiz-Cruz, M.D. and Sanz de Galdeano, C. (2013) Coesite and diamond inclusions, exsolution
1000 microstructures and chemical patterns in ultrahigh pressure garnet from Ceuta (Northern Rif,
1001 Spain). Lithos, 177, 184-206.

1002 Sack, R.O. and Ghiorso, M.S. (1991) An internally consistent model for the thermodynamic
1003 properties of Fe–Mg-titanomagnetite-aluminate spinels. Contributions to Mineralogy and
1004 Petrology, 106, 474-505.

1005 Sack, R.O. and Ghiorso, M.S. (1991) Chromian spinels as petrogenetic indicators:
1006 Thermodynamics and petrological applications. American Mineralogist, 76, 827-847.

1007 Sakamaki, K., Sato, Y. and Ogasawara, Y. (2016) Hydrous Na-garnet from Garnet Ridge;
1008 products of mantle metasomatism underneath the Colorado Plateau. Progress in Earth and
1009 Planetary Science, 3:20.

1010 Schreyer, W., Horrocks, P.C. and Abraham, K. (1984) High-magnesium staurolite in a
1011 sapphirine-garnet rock from the Limpopo Belt, Southern Africa. Contributions to Mineralogy
1012 and Petrology, 86, 200-207.

1013 Schumacher, J.C., Schumacher, R. and Robinson, P. (1989) Acadian metamorphism in central
1014 Massachusetts and south-western New Hampshire: evidence for contrasting *P-T* trajectories.
1015 In J.S. Daly, R.A. Cliff and B.W.D. Yardley, Eds., Evolution of Metamorphic Belts,
1016 Geological Society Special Publication, 43, 453-460.

1017 Sengupta, P., Sen, J., Dasgupta, S., Raith, M., Bhui, U.K. and Ehl, J. (1999) Ultra-high
1018 Temperature Metamorphism of Metapelitic Granulites from Kondapalle, Eastern Ghats Belt:
1019 Implications for the Indo-Antarctic Correlation. Journal of Petrology, 40, 1065-1087.

1020 Shaffer, M., Hacker, B.R., Ratschbacher, L., and Kylander-Clark, A.R.C. (2017) Foundering
1021 Triggered by the Collision of India and Asia Captured in Xenoliths. Tectonics, 36, 1913-
1022 1933.

1023 Shimpo, M., Tsunogae, T. and Santosh, M. (2006) First report of garnet-corundum rocks from
1024 southern India: Implications for prograde high-pressure (eclogite-facies?) metamorphism.
1025 Earth and Planetary Science Letters, 242, 111-129.

1026 Shulters, J.C. and Bohlen, S.R. (1989) The Stability of Hercynite and Hercynite-Gahnite Spinels
1027 in Corundum- or Quartz-Bearing Assemblages. Journal of Petrology, 30, 1017-1031.

1028 Smithies, R.H. and Champion, D.C. (1999) Late Archean felsic alkaline igneous rocks in the
1029 Eastern Goldfields, Yilgarn Craton, Western Australia: a result of lower crustal
1030 delamination? Journal of the Geological Society, London, 156, 561-576.

1031 Snoeyenbos, D.R. and Koziol, A.M. (2008) Exsolution Phenomena of UHP Type in Garnets
1032 From Western New England, USA. American Geophysical Union, Fall Meeting 2008,
1033 Abstract V31E-07.

1034 Snoeyenbos, D.R., Williams, M.L. and Hanmer, S. (1995) Archean high-pressure metamorphism
1035 in the western Canadian Shield. European Journal of Mineralogy, 7, 1251-1272.

1036 Sorger, D., Hauzenberger, C.A., Linner, M., Iglseder, C. and Finger, F. (2018). Carboniferous
1037 polymetamorphism recorded in paragneiss-migmatites from the Bavarian Unit (Moldanubian
1038 Superunit, Upper Austria): implications for the tectonothermal evolution at the end of the
1039 Variscan orogeny. Journal of Petrology, egy063.

1040 Štípská, P. and Powell, R. (2005) Does ternary feldspar constrain the metamorphic conditions of
1041 high-grade meta-igneous rocks? Evidence from orthopyroxene granulites, Bohemian Massif.
1042 Journal of Metamorphic Geology, 23, 627-647.

1043 Tchameni, R., Mezger, K., Nsifa, N.E. and Pouclet, A. (2001) Crustal origin of Early Proterozoic
1044 syenites in the Congo Craton (Ntem Complex), South Cameroon. Lithos, 57, 23-42.

1045 Thomson, J.A. (2001) A counterclockwise P-T path for anatectic pelites, south-central
1046 Massachusetts. Contributions to Mineralogy and Petrology, 141, 623-641.

1047 Tracy, R.J., Robinson, P, and Thompson, A.B. (1976) Garnet composition and zoning in the
1048 determination of temperature and pressure of metamorphism, central Massachusetts.
1049 American Mineralogist, 61, 762-775.

van Roermund, H.L.M., Drury, M.R., Barnhoorn, A. and De Ronde, A. (2000) Non-silicate inclusions in garnet from an ultra-deep orogenic peridotite. Geological Journal, 35, 209-229.

Weller, O.M. and St-Onge, M.R. (2017) Record of modern-style plate tectonics in the Palaeoproterozoic Trans-Hudson orogen. Nature Geoscience, 10, 305-311.

Wheller, C.J. and Powell, R. (2014) A new thermodynamic model for sapphirine: calculated phase equilibria in K_2O–FeO–MgO–Al_2O_3–SiO_2–H_2O–TiO_2–Fe_2O_3. Journal of Metamorphic Geology, 32, 287-299.

White, R.W., Powell, R. and Clarke, G.L. (2002) The interpretation of reaction textures in Fe-rich metapelitic granulites of the Musgrave Block, central Australia: constraints from mineral equilibria calculations in the system K_2O–FeO–MgO–Al_2O_3–SiO_2–H_2O–TiO_2–Fe_2O_3. Journal of Metamorphic Geology, 20, 41-55.

White, R.W., Powell, R., Holland, T.J.B., Johnson, T.E. and Green, E.C.R. (2014) New mineral activity-composition relations for thermodynamic calculations in metapelitic systems. Journal of Metamorphic Geology, 32, 261-286.

White, R.W., Powell, R. & Johnson, T.E. (2014) The effect of Mn on mineral stability in metapelites revisited: new *a-x* relations for manganese-bearing minerals. Journal of Metamorphic Geology, 32, 809-828.

Willner, A.P., Rötzler, K. and Maresch, W.V. (1997) Pressure-Temperature and Fluid Evolution of Quartzo-Feldspathic Metamorphic Rocks with a Relic High-Pressure, Granulite-Facies History from the Central Erzgebirge (Saxony, Germany). Journal of Petrology, 38, 307-336.

1070 Wintsch, R.P., Aleinikoff, J.N. and Walsh, G.J. (2009) Late Silurian Deposition and Late
1071 Devonian Metamorphism of Gander Cover at the Southern end of the Central Maine Terrane:
1072 Evidence from SHRIMP Analysis of Detrital Zircons. Geological Society of America
1073 Abstracts with Programs, 41, 98.

1074 Wintsch, R.P., Sutter, J.F., Kunk, M.J., Aleinikoff, J.N. and Dorais, M.J. (1992) Contrasting P-T-
1075 t Paths: Thermochronologic Evidence for a Late Paleozoic Final Assembly of the Avalon
1076 Composite Terrane in the New England Appalachians. Tectonics, 11, 672-689.

1077 Wu, C. and Chen, H. (2015) Revised Ti-in-biotite geothermometer for ilmenite- or rutile-bearing
1078 crustal metapelites. Science Bulletin, 60, 116-121.

1079 Yao, Y., Ye, K., Liu, J., Cong, B. and Wang, Q. (2000) A transitional eclogite- to high pressure
1080 granulite-facies overprint on coesite-eclogite at Taohang in the Sulu ultrahigh-pressure
1081 terrane, Eastern China. Lithos, 52, 109-120.

1082 Ye, K., Cong, B. and Ye, D. (2000) The possible subduction of continental material to depths
1083 greater than 200 km. Nature, 407, 734-736.

1084 Zegers, T.E. and van Keken, P.E. (2001) Middle Archean continent formation by crustal
1085 delamination. Geology, 29, 1083-1086.

1086 Zhang, R.Y., Zhai, S.M., Fei, Y.W. and Liou, J.G. (2003) Titanium solubility in coexisting
1087 garnet and clinopyroxene at very high pressure: the significance of exsolved rutile in garnet.
1088 Earth and Planetary Science Letters, 216, 591-601.

1089 Zhao, G., Cawood, P.A., Wilde, S.A. and Lu, L. (2001) High-Pressure Granulites (Retrograded
1090 Eclogites) from the Hengshan Complex, North China Craton: Petrology and Tectonic
1091 Implications. Journal of Petrology, 42, 1141-1170.

1092 Zulauf, G., Dörr, W., Fiala, J., Kotková, J., Maluski, H. and Valverde-Vaquero, P. (2002)
1093 Evidence for high-temperature diffusional creep preserved by rapid cooling of lower crust
1094 (North Bohemian shear zone, Czech Republic). Terra Nova, 14, 343-354.

This is a preprint, the final version is subject to change, of the American Mineralogist (MSA)
Cite as Authors (Year) Title. American Mineralogist, in press.
DOI: https://doi.org/10.2138/am-2018-6543

1095 **FIGURE 1**: Geologic map showing (**a**) Major geologic terranes of New England, U.S.A.
1096 following Axler (unpublished PhD thesis; after Aleinikoff et al (2007) as modified from Hibbard
1097 et al. (2006)). (**b**) Sample location within thrust slices of the Central Maine Terrane. Formations
1098 colored in red are UHT (Ague et al. 2013; Axler and Ague 2015a; based on geologic maps of
1099 Rodgers 1981,1985). HB=Hartford Basin, RH=Rowe-Hawley, P-N=Putnam-Nashoba.

1100 **FIGURE 2**: Field exposures of the silica-undersaturated rocks. Grt = garnet. (**a**) Sheared
1101 leucosome; arrows indicate thrust sense of shear. (**b**) Garnet megacrysts surrounded by
1102 leucosome.

1103 **FIGURE 3**: Silica-undersaturated rocks in hand sample. Grt = garnet, spl = spinel, crn =
1104 corundum, fsp = feldspar. (**a**) Type II sample showing coarse leucosomes and spinel defining
1105 foliation and pink-purple sapphires within leucosomes [296A]. (**b**) Peritectic garnet including
1106 antiperthite surrounded by antiperthite-bearing leucosome in contact with a pink sapphire; spinel
1107 and corundum are present in the matrix assemblage [295A]. (**c**) Spinel mass showing irregular
1108 crystallographic domains revealed by differential reflection of light [296A]. (**d**) Concentrically
1109 zoned sapphire in contact with leucosome and garnet that includes pink corundum [298A]. (**e**)
1110 Type I sample [150A].

1111 **FIGURE 4**: Photomicrographs of representative garnet textures in thin section. Grt = garnet, spl =
1112 spinel, crn = corundum, bt = biotite, rt = rutile, sill = sillimanite, ilm = ilmenite, ap = apatite. (**a**)
1113 Matrix assemblage with typical porphyroblastic garnet and second-generation euhedral garnets,
1114 as well as spinel (dark) rimmed by corundum; plane light [268A-2]. (**b**) Garnet with sillimanite
1115 inclusions (core) and spinel inclusions (rim) reflecting a granulite facies assemblage; plane light
1116 [296A-3]. (**c**) Oriented rutile needles in the core of high-phosphorus garnet (Fig. 6; Table 2),

This is a preprint, the final version is subject to change, of the American Mineralogist (MSA)
Cite as Authors (Year) Title. American Mineralogist, in press.
DOI: https://doi.org/10.2138/am-2018-6543

crossed polars [294A-2]. (**d**) Oriented rutile needles with composite needles of ilmenite and apatite in the same garnet core; plane light [294A-2].

FIGURE 5: Spinel and corundum. Grt = garnet, spl = spinel, crn = corundum, ilm = ilmenite, bt = biotite. (**a**) Photomicrograph of ragged spinel and rounded biotite inclusions in a garnet core; plane light [296A-3]. (**b**) Photomicrograph of corundum with biotite inclusions cross-cutting and rimming spinel; plane light [296A-3E2]. (**c**) Photomicrograph (true color) of oriented Fe-Ti oxide lamellae in spinel; a domain boundary is marked by the change in lamellae orientation, condenser lens in, plane light [296A-3]. (**d**) Element map of Ti in spinel showing orientations of ilmenite lamellae; brighter colors indicate higher concentration [294B]. (**e**) Element map of Cr in a pink corundum in leucosome showing concentric euhedral growth zoning [295A-1].

FIGURE 6: Element maps of the high-phosphorus garnet of 294A-1. Ap = apatite, kfs = K-feldspar. (**a**) and (**b**) Phosphorus. (**c**): Magnesium. (**d**) Calcium. (**e**) Backscattered electron image. Warmer colors indicate higher concentration. Color scale does not correlate across panels. Black arrow in inset panel indicates the region with measured 0.18 wt% P_2O_5 (Table 2).

FIGURE 7: Feldspar textures. Grt = garnet, anti = antiperthite, kfs = K-feldspar, ap = apatite, plag = plagioclase. (**a**) Leucosome in contact with peritectic garnet [295A]. (**b**) Oriented apatite needles in perthite [294A-5]. (**c**) Perthite showing characteristic lack of exsolution lamellae in the rim, crossed polars [294A-1]. (**d**) Backscattered electron image of perthite (Sample T) showing plagioclase clustered along cracks and at grain boundaries [278A-1] (**e**) Composite backscattered electron image of antiperthites with coarse exsolution lamellae approaching 1 mm in length [278A-1] (**f**) Enlarged view of a K-feldspar lamellae in antiperthite of panel **e**, showing exsolution lamellae of plagioclase.

This is a preprint, the final version is subject to change, of the American Mineralogist (MSA)
Cite as Authors (Year) Title. American Mineralogist, in press.
DOI: https://doi.org/10.2138/am-2018-6543

FIGURE 8: Photomicrograph of texturally late sillimanite in thin section cross-cutting foliation; crossed polars [269A-1].

FIGURE 9: Results of ternary feldspar reintegration thermometry for antiperthites (numbers) and perthites (letters) plotted on the feldspar ternary diagram. Temperature contours are from the feldspar activity models of Benisek et al. (2010) and Benisek et al. (2004). Sample codes 1-6 correspond to samples 150A-2, 271A-1, 278A-1 (3-5), and 281A-1 respectively. Sample codes A-F correspond to samples 294A-1 (A-C), 294A-3, and 312A-1(2x) respectively. Points E and F overlap. Points B and C come from different regions of the same grain. Point T is the perthite pictured in Fig. 7d, reintegrated to include grain boundary plagioclase, for which host and lamellae compositions are given in Table 9. Temperature estimates are given in Table 10. White dotted line indicates the tie line for reintegrated antiperthite and perthite including grain boundary plagioclase from the same sample.

FIGURE 10: Pseudosections constructed for samples 150A, 268A, and 269A. Grt = garnet, crn = corundum, cpx = clinopyroxene, wm = white mica, bi = biotite, ksp = K-feldspar, ilm = ilmenite, plag = plagioclase, sill = sillimanite, spl = spinel, ky = kyanite, lc = leucite, rt = rutile, gro = grossular. Yellow band shows the mean ±2σ standard error of the antiperthite temperatures of all analyses (Table 6) using the feldspar activity models of Benisek et al. (2004) and Benisek et al. (2010).

Table 1. Bulk compositions of samples used for pseudosection modeling

	Type I	Type II	
	150A	268A	269A
SiO_2 (wt%)	38.63	40.80	44.10
TiO_2	2.38	2.18	1.94
Al_2O_3	27.69	24.90	23.00
FeO(tot)	18.74	17.38	16.39
Fe_2O_3	0.21	0.19	0.18
FeO	18.53	17.19	16.21
MgO	2.94	4.01	3.60
MnO	0.19	0.07	0.07
CaO	0.74	0.32	0.88
Na_2O	0.65	0.66	1.16
K_2O	6.19	7.97	7.39
P_2O_5	0.35	0.14	0.13
LOI	1.79	2.15	2.12
Total	99.94	100.44	100.65
mol Fe^{3+}/Fe(tot)	0.01	0.01	0.01
Density @ 1040 ºC, 1.8 GPa (g/cm^3)	3.09	2.98	2.95
Density (-50% melt)	3.25	3.09	3.05
Density (-100% melt)	3.52	3.26	3.22

Notes: Compositions were obtained by X-ray fluorescence (XRF). CaO adjusted assuming all P_2O_5 is hosted in apatite. LOI denotes loss on ignition, and is re-calculated from raw values to account for Fe_2O_3 created during XRF combustion assuming Fe^{3+}/Fe(tot) ratio of 0.01 (see Analytical Methods). Densities calculated using Theriak-Domino.

Table 2. Garnet analyses

Sample	150A-3 Core	150A-3 Rim	268A-1 Gt_{II} Core	268A-2 Core	268A-2 Rim	269A-1 Core	269A-1 Rim	294A-1 Core	150A-3 Range *n=13*	268A-1 Gt_{II} Range *n=10*	268A-2 Range *n=6*	269A-1 Range *n=11*
SiO_2 (wt%)	37.86	37.32	37.40	38.01	37.30	37.88	37.10	37.10	1.16	0.26	0.71	1.04
TiO_2	0.06	0.01	0.01	0.01	0.03	b.d.	0.05	0.04	0.06	0.03	0.07	0.05
P_2O_5	0.04	0.03	0.05	0.05	0.02	0.03	0.03	0.18	0.02	0.02	0.07	0.04
Al_2O_3	21.35	21.00	21.24	21.47	21.14	21.50	20.97	21.16	0.70	0.10	0.50	0.68
Cr_2O_3	0.05	0.01	0.05	0.03	0.04	0.05	0.05	0.09	0.07	0.05	0.05	0.03
FeO(tot)	34.44	36.73	37.80	35.13	37.91	34.59	37.24	36.60	4.01	0.81	3.62	3.53
MgO	4.79	3.36	2.95	4.73	2.64	4.79	2.87	3.90	2.55	0.24	2.09	2.43
MnO	0.93	0.52	0.16	0.46	0.29	0.38	0.41	0.25	0.45	0.06	0.29	0.11
CaO	1.62	1.29	0.98	1.39	1.48	1.34	1.47	1.16	0.74	0.31	0.48	0.18
Na_2O	0.03	0.01	0.02	0.01	0.01	0.01	b.d.	0.02	0.02	0.01	0.01	0.01
Total	101.17	100.28	100.66	101.33	100.86	100.57	100.19	100.50				
Structural Formulas (12 O)												
Si	2.979	2.994	3.000	2.989	2.991	2.997	2.990	2.962				
Ti	0.004		0.001	0.001	0.002		0.003	0.002				
P	0.003	0.002	0.003	0.004	0.001	0.002	0.002	0.012				
Al	1.980	1.985	2.008	1.990	1.998	2.005	1.992	1.991				
Cr	0.003		0.003	0.002	0.003	0.003	0.003	0.006				
Fe^{3+}	0.048	0.024		0.021	0.012		0.012	0.042				
Fe^{2+}	2.219	2.441	2.553	2.289	2.530	2.295	2.498	2.401				
Mg	0.562	0.402	0.353	0.555	0.316	0.565	0.345	0.464				
Mn	0.062	0.035	0.011	0.031	0.020	0.025	0.028	0.017				
Ca	0.137	0.111	0.084	0.117	0.127	0.113	0.127	0.099				
Na	0.005	0.001	0.003	0.002	0.002	0.001		0.004				

Notes: b.d. = below detection. Structural formula Fe^{2+} and Fe^{3+} calculated using 8 cations and 12 oxygens. Gt_{II} is the second generation noted in the Results section of the text. Range denotes the difference between maximum and minimum values across all grains.

Table 3. Spinel analyses

Sample	268A-1 Core	268A-1 Rim	268A-2 Grt incl	269A-1 Core	269A-1 Rim	294A-1 Core	294A-1 Rim	277A-3 Reint core *n=25*	268A-1 Range *n=13*	269A-1 Range *n=7*	294A-1 Range *n=11*
SiO_2(wt%)	b.d.	0.07	0.02	0.01	b.d.	b.d.	0.02	b.d.	0.06	0.05	0.03
TiO_2	0.02	0.04	0.01	0.01	0.02	0.21	0.09	0.10	0.09	0.06	0.21
Al_2O_3	56.30	56.03	57.70	56.16	56.09	55.58	52.62	56.59	1.39	0.96	3.26
Cr_2O_3	0.67	1.18	0.93	0.92	1.29	1.41	4.39	0.06	0.76	0.98	4.07
FeO(tot)	40.38	39.42	36.28	39.05	39.00	39.60	39.23	39.40	1.17	1.62	1.84
Fe_2O_3	4.02	2.74	2.48	3.26	2.85	2.87	2.74	3.91			
FeO	36.76	36.96	34.05	36.12	36.43	37.01	36.76	35.88			
MgO	2.68	2.27	4.49	2.81	2.62	2.38	2.01	3.26	0.59	0.39	0.60
MnO	b.d.	b.d.	0.01	0.01	b.d.	b.d.	0.07	0.01	0.04	0.08	0.07
NiO	0.14	0.11	0.15	0.11	0.13	0.13	0.04	0.09	0.12	0.08	0.15
ZnO	0.21	0.42	0.12	0.36	0.29	0.17	0.21	0.08	0.26	0.16	0.14
V_2O_3	0.06	0.07	0.06	0.10	0.06	0.06	0.06	0.04	0.03	0.05	0.05
Total	100.86	99.93	100.02	99.87	99.79	99.83	99.01	100.02			
Structural formulas (4 O)											
Si		0.002	0.001				0.001				
Ti		0.001				0.005	0.002	0.002			
Al	1.896	1.906	1.923	1.905	1.906	1.895	1.830	1.909			
Cr	0.015	0.027	0.021	0.021	0.029	0.032	0.102	0.001			
Fe^{3+}	0.086	0.059	0.053	0.071	0.062	0.063	0.061	0.084			
Fe^{2+}	0.879	0.892	0.805	0.870	0.879	0.895	0.907	0.859			
Mg	0.114	0.098	0.189	0.121	0.113	0.103	0.088	0.139			
Mn							0.002				
Ni	0.003	0.003	0.003	0.003	0.003	0.003	0.001	0.002			
Zn	0.004	0.009	0.003	0.008	0.006	0.004	0.005	0.002			
V	0.001	0.002	0.001	0.002	0.001	0.001	0.001	0.001			

Notes: b.d. = below detection. FeO and Fe_2O_3 wt% and Fe^{2+} and Fe^{3+} in structural formulas calculated using 3 cations and 4 oxygens. Range denotes the difference between maximum and minimum values across all grains.

Table 4. Corundum and ilmenite analyses

Sample	296A-3 crn	296A-4A crn	150A-3 ilm	268A-2 ilm	269A-1 ilm	294A ilm
SiO_2	b.d.	b.d.	b.d.	0.05	0.05	0.05
TiO_2	0.01	0.03	51.93	52.08	51.95	50.20
Al_2O_3	100.60	99.74	0.04	0.03	0.03	0.05
Cr_2O_3	0.03	0.17	0.01	b.d.	b.d.	0.08
V_2O_3	b.d.	b.d.	0.37	0.34	0.22	b.d.
FeO(tot)	0.30	0.83	47.64	47.50	47.00	47.66
Fe_2O_3	0.33	0.98	1.48	1.07	0.54	4.18
FeO			46.31	46.53	46.52	43.89
MgO	b.d.	b.d.	0.15	0.18	0.06	0.70
MnO	0.01	b.d.	0.07	0.01	0.12	0.03
NiO	b.d.	b.d.	0.02	0.02	b.d.	0.01
ZnO	b.d.	0.01	0.04	b.d.	0.05	b.d.
CaO	b.d.	0.06	b.d.	0.01	b.d.	0.04
Total	100.98	100.99	100.43	100.30	99.53	99.22
Structural formulas (3 O)						
Si				0.001	0.001	0.001
Ti			0.982	0.985	0.991	0.957
Al	1.995	1.984	0.001	0.001	0.001	0.002
Cr		0.002				0.002
V			0.008	0.007	0.005	
Fe^{3+}	0.004	0.012	0.028	0.020	0.010	0.080
Fe^{2+}			0.973	0.979	0.986	0.931
Mg			0.006	0.007	0.002	0.026
Mn			0.002		0.003	0.001
Ni						
Zn			0.001		0.001	
Ca		0.001				0.001

Notes: b.d. = below detection. FeO and Fe_2O_3 wt% and structural formula Fe^{2+} and Fe^{3+} calculated using 2 cations and 3 oxygens.

Table 5. Biotite analyses

Sample	150A-3	268A-1	268A-1	269A-1	269A-1	294A-1	294A-1
SiO_2 (wt%)	34.40	34.86	34.84	33.79	34.28	33.85	34.57
TiO_2	2.83	4.02	4.49	4.72	4.71	4.84	6.61
Al_2O_3	20.17	19.75	17.95	18.07	18.22	18.17	16.94
Cr_2O_3	0.11	0.20	0.11	0.16	0.14	0.17	0.22
FeO	22.45	14.66	20.91	21.53	21.99	23.54	21.00
MgO	7.53	12.71	8.94	7.81	7.73	6.95	8.09
MnO	b.d.	0.07	b.d.	0.07	b.d.	0.05	b.d.
NiO	0.13	0.05	b.d	0.05	0.06	0.06	b.d.
ZnO	b.d.	b.d.	b.d.	b.d.	b.d.	b.d.	0.02
BaO	0.11	0.10	0.11	0.10	0.12	0.09	0.11
Na_2O	0.07	0.35	0.12	0.13	0.09	0.11	0.18
K_2O	9.37	9.65	9.77	9.67	9.84	9.73	9.66
F	0.10	0.28	0.22	0.19	0.16	0.06	0.22
Cl	0.02	0.01	0.01	0.03	0.02	0.06	0.01
Total	97.23	96.58	97.39	96.23	97.29	97.63	97.53
			Structural formulas (11 O)				
Si	2.606	2.570	2.627	2.596	2.606	2.587	2.611
Ti	0.161	0.223	0.255	0.273	0.270	0.278	0.375
Al	1.801	1.716	1.595	1.635	1.633	1.636	1.508
Cr	0.006	0.012	0.007	0.009	0.008	0.010	0.013
Fe^{2+}	1.422	0.904	1.318	1.383	1.398	1.504	1.326
Mg	0.850	1.397	1.005	0.895	0.876	0.792	0.910
Mn		0.004		0.004		0.003	
Ni		0.003		0.003	0.004	0.004	
Zn							0.001
Ba	0.003	0.003	0.003	0.003	0.004	0.003	0.003
Na	0.010	0.049	0.017	0.020	0.014	0.016	0.027
K	0.905	0.908	0.940	0.947	0.955	0.947	0.931
F	0.024	0.065	0.053	0.046	0.039	0.016	0.053
Cl	0.002	0.002	0.001	0.004	0.003	0.008	0.002

Note: b.d. = below detection. The analysis from sample 294A-1 with the highest Ti is an inclusion in the core of the garnet with 0.18 wt% P_2O_5 (294A-1 Core in Table 2). All Fe as FeO.

Table 6. Host compositions from reintegrated antiperthites

Sample	150A-2 *n=10*	271A-1 *n=10*	278A-1A *n=5*	278A-1B *n=5*	278A-1C *n=12*	281A-1 *n=5*
SiO_2	59.48(0.25)	57.24(0.16)	57.73(0.17)	57.93(0.18)	58.22(0.21)	58.28(0.16)
Al_2O_3	26.27(0.15)	27.53(0.19)	27.06(0.14)	26.92(0.05)	27.23(0.14)	27.04(0.07)
FeO	0.01(0.01)	0.03(0.03)	0.02(0.01)	0.03(0.03)	0.03(0.03)	0.04(0.04)
MgO	b.d.	0.01(0.01)	b.d.	b.d.	0.01(0.01)	0.02(0.01)
MnO	0.02(0.03)	0.01(0.02)	0.01(0.02)	0.01(0.03)	0.02(0.03)	0.01(0.02)
CaO	7.72(0.08)	9.39(0.10)	8.77(0.11)	8.65(0.12)	8.73(0.09)	8.54(0.10)
BaO	0.01(0.01)	0.01(0.01)	0.01(0.01)	0.02(0.01)	0.01(0.01)	0.01(0.01)
Na_2O	6.99(0.10)	6.11(0.09)	6.41(0.10)	6.42(0.06)	6.48(0.09)	6.56(0.08)
K_2O	0.20(0.01)	0.19(0.02)	0.21(0.01)	0.20(0.03)	0.21(0.02)	0.20(0.02)
Total	100.7(0.41)	100.51(0.31)	100.21(0.18)	100.18(0.25)	100.92(0.22)	100.70(0.15)
Structural formulas (8 O)						
Si	2.635	2.554	2.579	2.588	2.582	2.589
Al	1.372	1.448	1.425	1.417	1.423	1.416
Fe		0.001	0.001	0.001	0.001	0.002
Mg						0.001
Mn	0.001	0.001			0.001	
Ca	0.366	0.449	0.420	0.414	0.415	0.407
Ba						
Na	0.600	0.529	0.555	0.556	0.557	0.565
K	0.011	0.011	0.012	0.011	0.012	0.011

Notes: b.d. = below detection. 2σ standard deviations given in parentheses. All Fe as FeO.

Table 7. Exsolution lamellae compositions from reintegrated antiperthites

Sample	150A-2 *n=12*	271A-1 *n=10*	278A-1A *n=17*	278A-1B *n=12*	278A-1C *n=26*	281A-1 *n=8*
SiO_2	64.40(0.29)	65.37(0.20)	64.90(0.3)	65.32(0.27)	65.59(0.54)	64.88(0.17)
Al_2O_3	18.87(0.13)	18.79(0.15)	18.82(0.19)	18.77(0.11)	18.85(0.04)	19.01(0.11)
FeO	0.04(0.03)	0.02(0.02)	0.02(0.03)	0.02(0.02)	0.02(0)	0.05(0.03)
MgO	b.d.	b.d.	b.d.	b.d.	b.d.	b.d.
MnO	0.01(0.02)	0.02(0.02)	0.01(0.02)	0.02(0.03)	0.01(0)	0.01(0.01)
CaO	0.07(0.02)	0.07(0.01)	0.08(0.07)	0.07(0.02)	0.06(0.11)	0.07(0.01)
BaO	0.52(0.03)	0.20(0.02)	0.21(0.04)	0.12(0.02)	0.13(0.02)	0.79(0.04)
Na_2O	1.10(0.06)	1.01(0.03)	1.01(0.05)	1.01(0.03)	0.99(0.09)	1.17(0.06)
K_2O	14.80(0.10)	15.17(0.13)	15.12(0.18)	15.23(0.11)	15.18(0.09)	14.67(0.13)
Total	99.80(0.43)	100.65(0.35)	100.17(0.42)	100.56(0.32)	100.84(0.18)	100.65(0.17)
			Structural formulas (8 O)			
Si	2.978	2.992	2.986	2.992	2.994	2.978
Al	1.028	1.013	1.020	1.013	1.034	1.028
Fe	0.001	0.001	0.001	0.001	0.001	0.002
Mg						
Mn	0.001	0.001		0.001		
Ca	0.004	0.003	0.004	0.003	0.003	0.003
Ba	0.009	0.004	0.004	0.002	0.002	0.014
Na	0.098	0.090	0.090	0.090	0.087	0.104
K	0.873	0.886	0.887	0.890	0.884	0.859

Notes: b.d. = below detection. 2σ standard deviations given in parentheses. All Fe as FeO.

Table 8. Reintegrated perthite compositions measured by beam grids

Sample	294A-1* *n=25*	294A-1* *n=25*	294A-1 *n=25*	294A-3 *n=25*	312A-1 *n=25*	312A-1 *n=25*
SiO_2	64.30(0.35)	64.29(0.27)	64.34(0.35)	64.41(0.17)	64.10(0.35)	64.70(0.16)
P_2O_5	0.29(0.03)	0.34(0.04)	0.34(0.22)	0.25(0.03)	0.19(0.02)	0.20(0.03)
Al_2O_3	19.48(0.44)	19.39(0.31)	19.30(0.23)	19.19(0.10)	19.35(0.34)	19.61(0.17)
FeO	0.02(0.02)	0.02(0.03)	0.03(0.03)	0.04(0.03)	0.03(0.04)	0.09(0.03)
MgO	b.d.	b.d.	0.01(0.01)	b.d.	0.01(0.02)	0.02(0.01)
MnO	0.01(0.02)	0.01(0.02)	0.01(0.01)	0.01(0.02)	0.01(0.02)	0.01(0.02)
CaO	0.40(0.43)	0.28(0.30)	0.40(0.30)	0.22(0.04)	0.48(0.25)	0.45(0.12)
BaO	0.14(0.03)	0.15(0.03)	0.14(0.04)	0.19(0.03)	0.40(0.05)	0.38(0.04)
Na_2O	2.13(0.48)	1.96(0.32)	2.36(0.35)	1.76(0.06)	3.01(0.60)	3.08(0.35)
K_2O	13.43(1.03)	13.76(0.69)	13.17(0.59)	14.01(0.13)	12.02(1.01)	11.91(0.56)
Total	100.20(0.25)	100.20(0.23)	100.10(0.27)	100.09(0.22)	99.61(0.43)	100.45(0.19)
			Structural formulas (8 O)			
Si	2.943	2.945	2.946	2.957	2.945	2.944
P	0.011	0.013	0.013	0.010	0.007	0.008
Al	1.051	1.047	1.041	1.038	1.048	1.052
Fe	0.001	0.001	0.001	0.002	0.001	0.003
Mg					0.001	0.001
Mn					0.001	
Ca	0.020	0.014	0.020	0.011	0.024	0.022
Ba	0.003	0.003	0.003	0.003	0.007	0.007
Na	0.189	0.174	0.210	0.157	0.268	0.272
K	0.784	0.804	0.769	0.820	0.705	0.691

Notes: b.d. = below detection. 2σ standard deviations given in parentheses. All Fe as FeO. *Analyses come from two different portions of the same grain.

Table 9. Reintegrated perthite composition with grain boundary plagioclase

Sample	278A-1 host *n=5*	278A-1 lamellae *n=5*
SiO_2	65.32(0.14)	57.60(0.46)
Al_2O_3	18.71(0.15)	26.97(0.10)
FeO	0.01(0.02)	0.03(0.03)
MgO	b.d.	b.d.
MnO	0.01(0.02)	b.d.
CaO	0.06(0.02)	8.82(0.20)
BaO	0.20(0.03)	0.01(0.01)
Na_2O	1.10(0.06)	6.45(0.09)
K_2O	14.96(0.11)	0.21(0.03)
Total	100.37(0.27)	100.10(0.36)
	Structural formulas (8 O)	
Si	2.995	2.583
Al	1.011	1.418
Fe	0.001	0.001
Mg		
Mn		
Ca	0.003	0.421
Ba	0.004	
Na	0.098	0.558
K	0.875	0.012

Notes: b.d. = below detection. 2σ standard deviations given in parentheses. All Fe as FeO.

Table 10. Reintegrated ternary feldspar compositions plotted in Figure 9

	Perthite						
Sample	294A-1	294A-1	294A-1	294A-3	312A-1	312A-1	278A-1
Plotting Code	A	B	C	D	E	F	T
Kfs	79.0	81.0	77.0	83.1	70.2	70.7	77.3
Ab	19.0	17.6	21.0	15.9	27.6	26.9	16.5
An	2.0	1.4	2.0	1.1	2.2	2.4	6.2
T(°C) @ 1.5 GPa [B10]	893	848	885	822	874	886	1118
T(°C) @ 1.5 GPa [B04]	780	738	792	707	840	843	914
	Antiperthite						
Sample	150A-2	271A-1	278A-1	278A-1	278A-1	281A-1	
Plotting Code	1	2	3	4	5	6	
Kfs	16.1	22.8	18.9	19.3	23.2	18.3	
Ab	52.7	42.7	46.9	47.0	44.9	48.6	
An	31.2	34.5	34.2	33.7	31.9	33.1	
T(°C) @ 1.5 GPa [B10]	979	1114	1055	1054	1084	1034	
T(°C) @ 1.5 GPa [B04]	985	1050	1019	1022	1047	1012	
Two-feldspar *T*			1059	1058	1073/1081		

Notes: Abbreviations of feldspar models are B04 = Benisek et al. (2004) and B10 = Benisek et al. (2010). Perthite compositions are averages of grid analyses (Table 8) except 278A-1 plotting code T, which is based on spot analyses of host and grain boundary plagioclase (Table 9) reintegrated following the procedure used for antiperthite. K-feldspar (Kfs), albite (Ab), and anorthite (An) are given in mol%. Two-feldspar *T* estimates all use the same Kfs composition (278A-1 plotting code T). Plotting codes refer to Fig. 9.

Figure 1

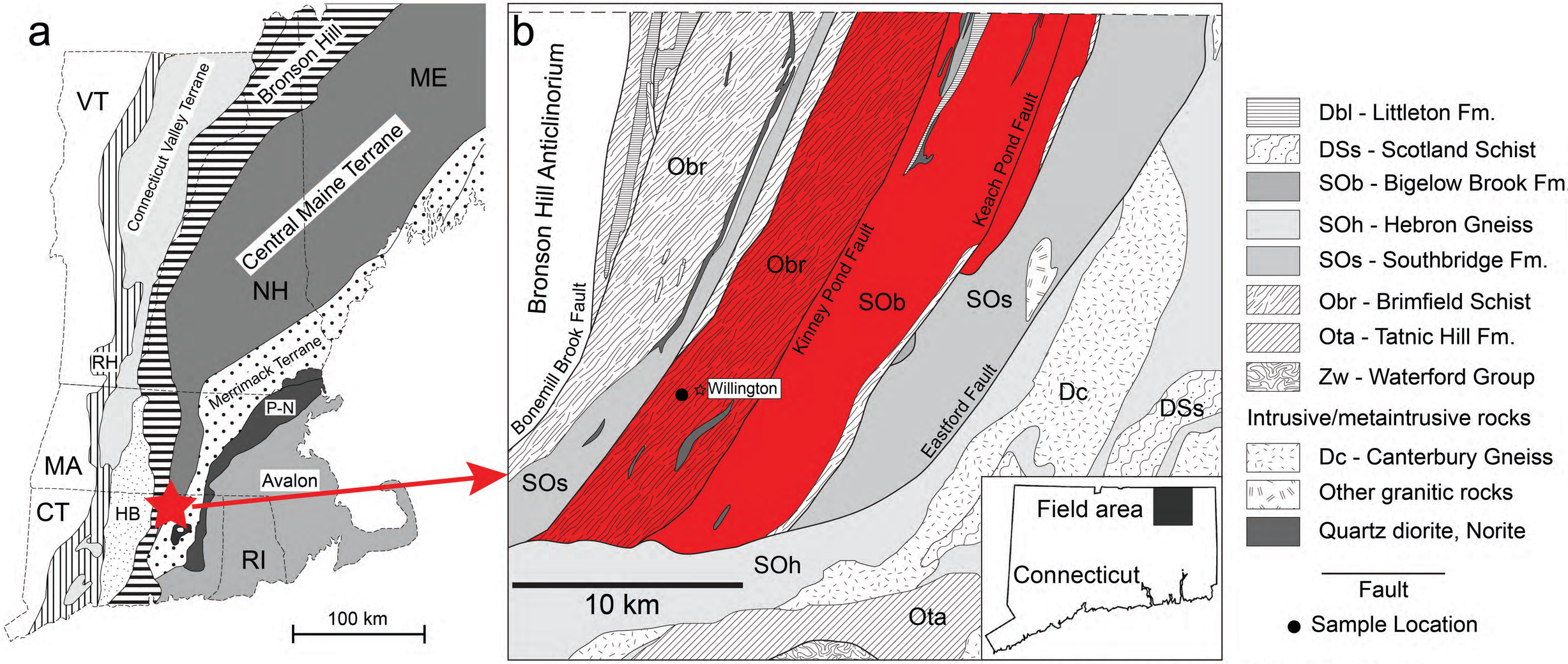

Ague & Eckert (2012 AmMin): Ague et al. (2013 Geology); Axler & Ague (2015a JMG, 2015b AmMin)

Figure 2

Figure 3

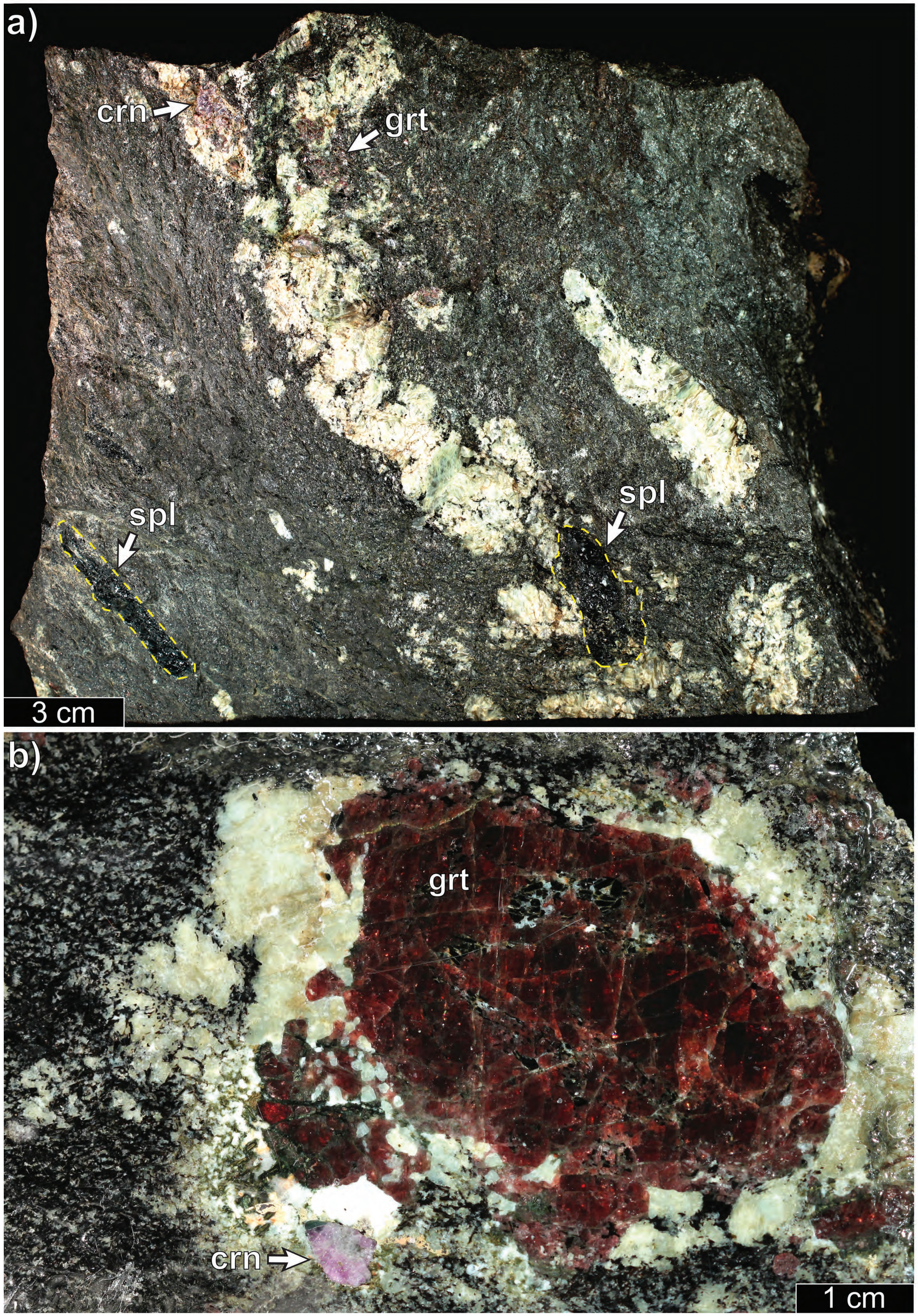
a)
crn
grt
spl
spl
3 cm

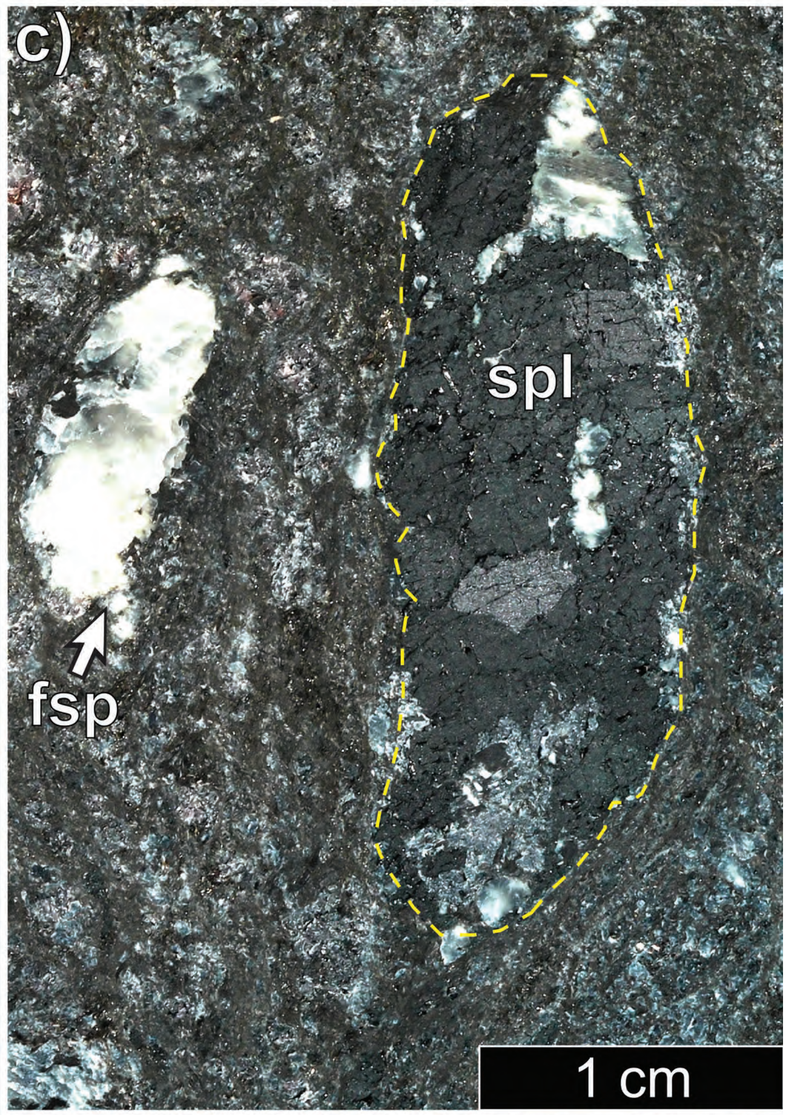
c)
spl
fsp
1 cm

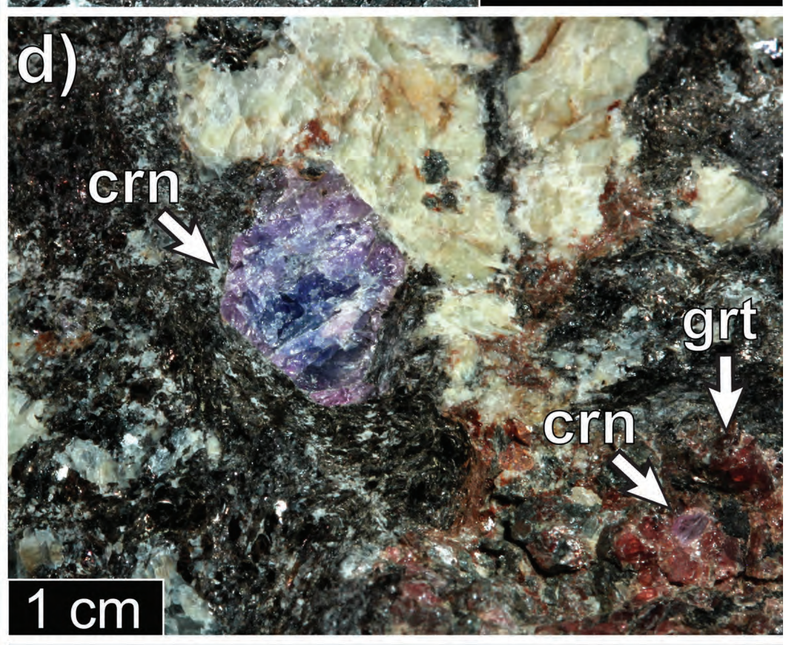
d)
crn
grt
crn
1 cm

b)
grt
crn
1 cm

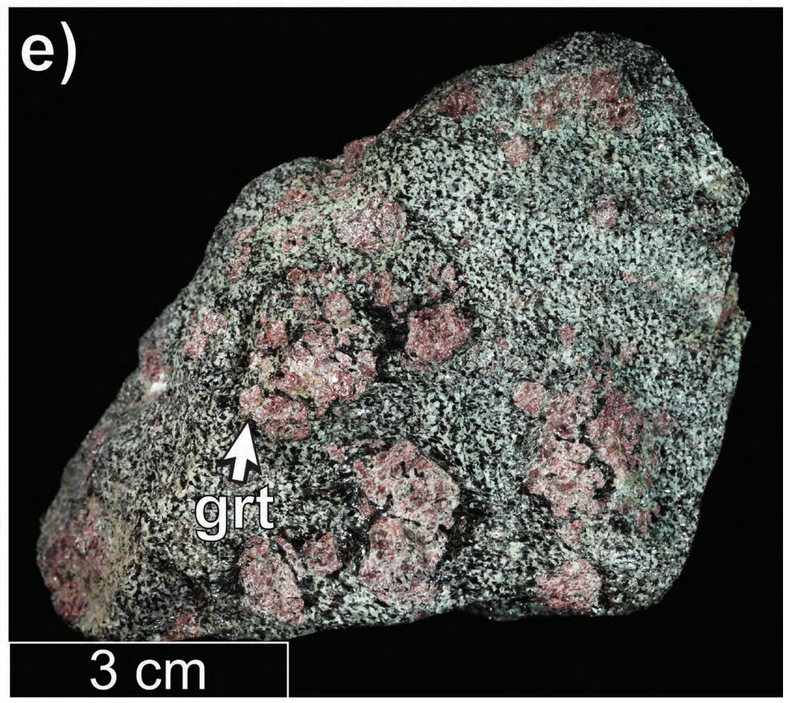
e)
grt
3 cm

Figure 4

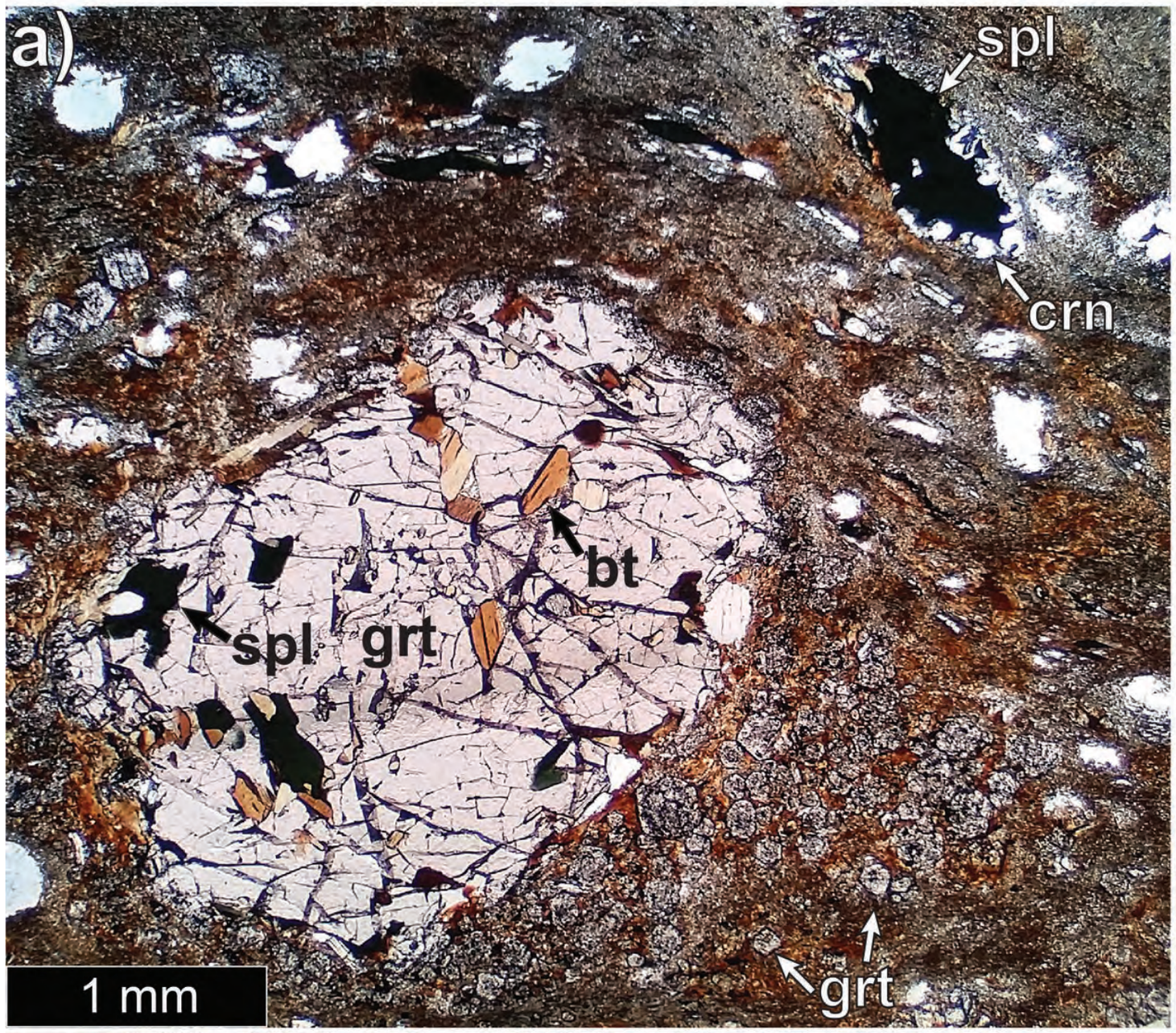
a)
spl
crn
bt
spl
grt
grt
1 mm

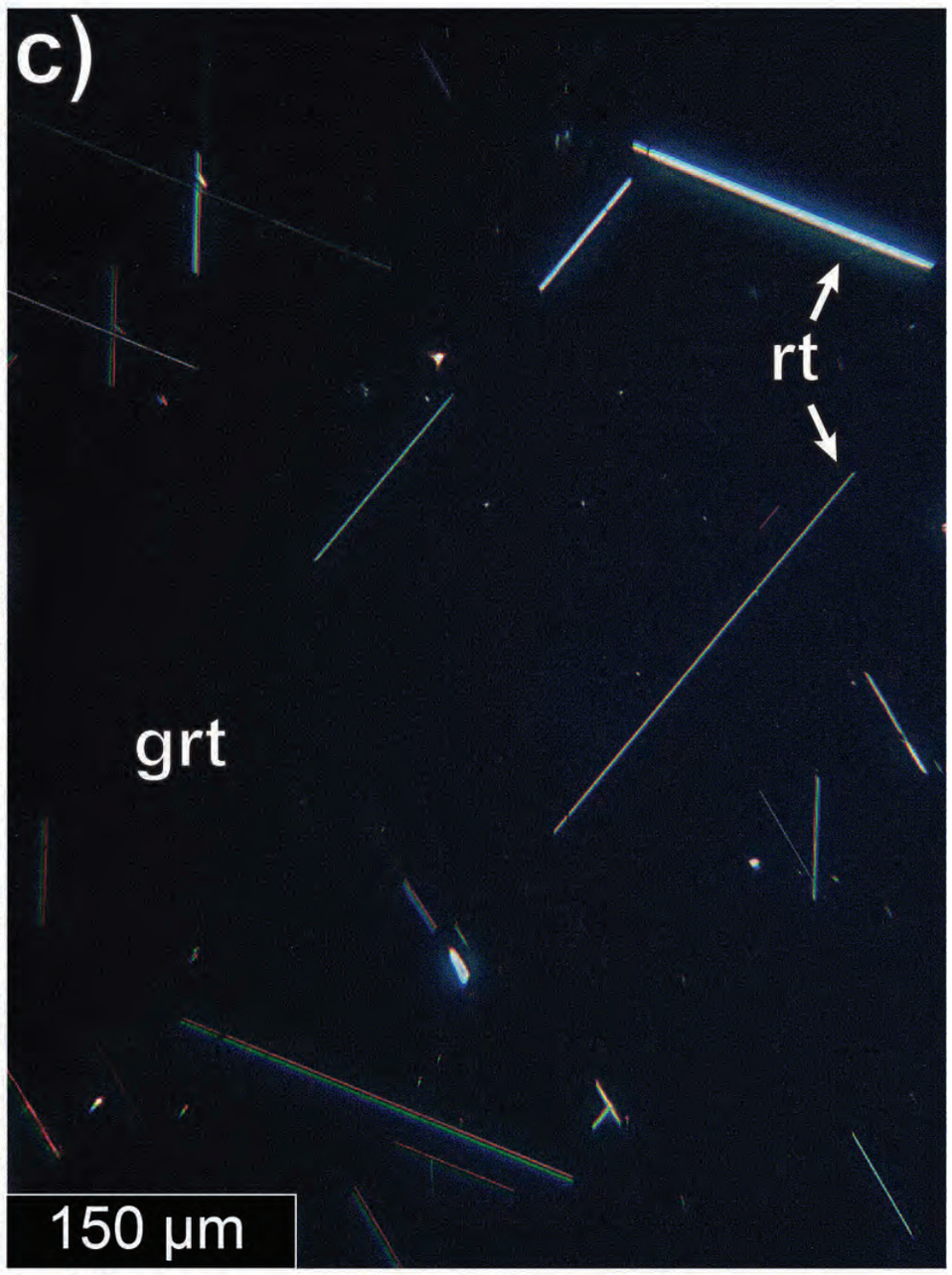
c)
rt
grt
150 µm

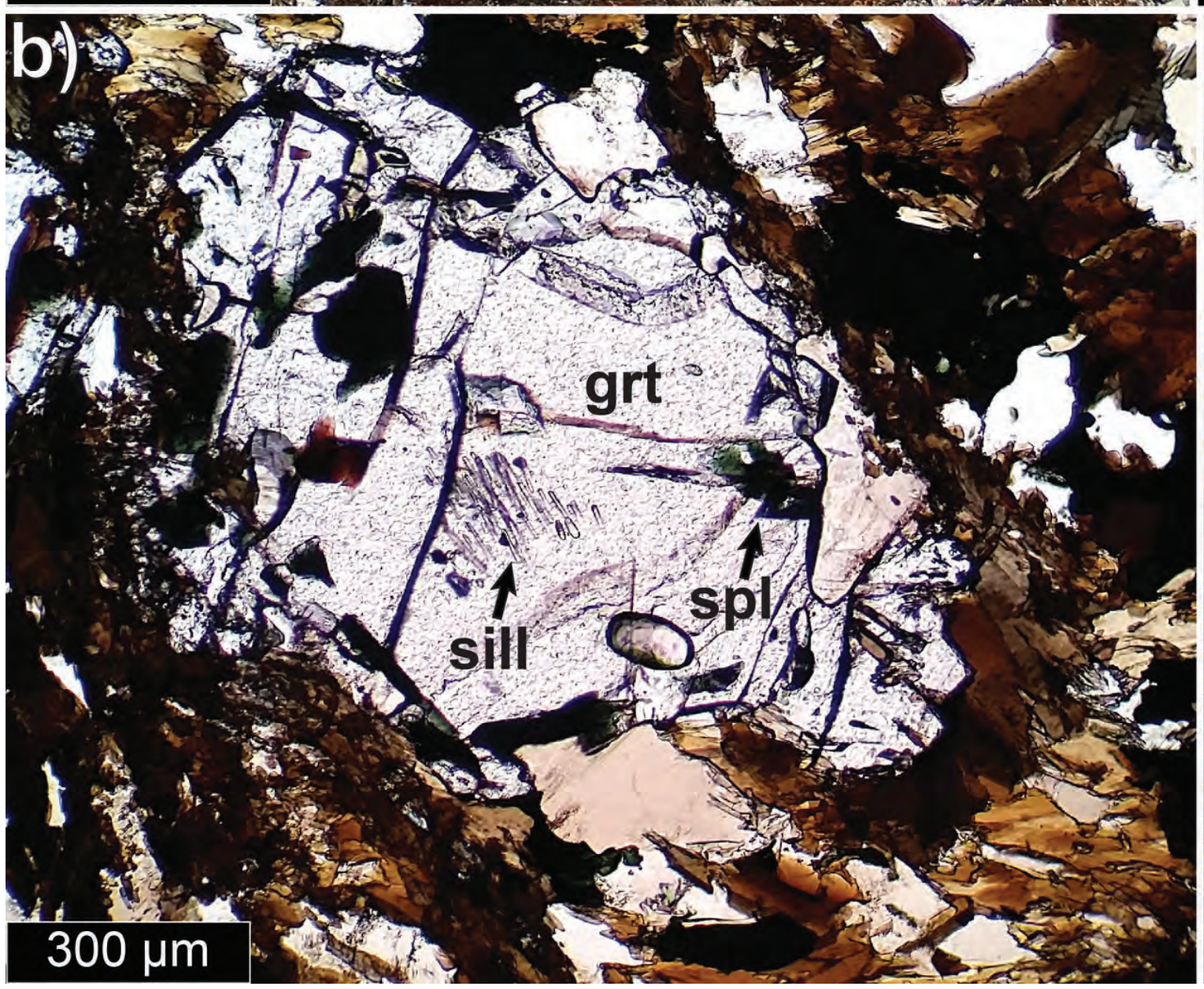
b)
grt
sill
spl
300 µm

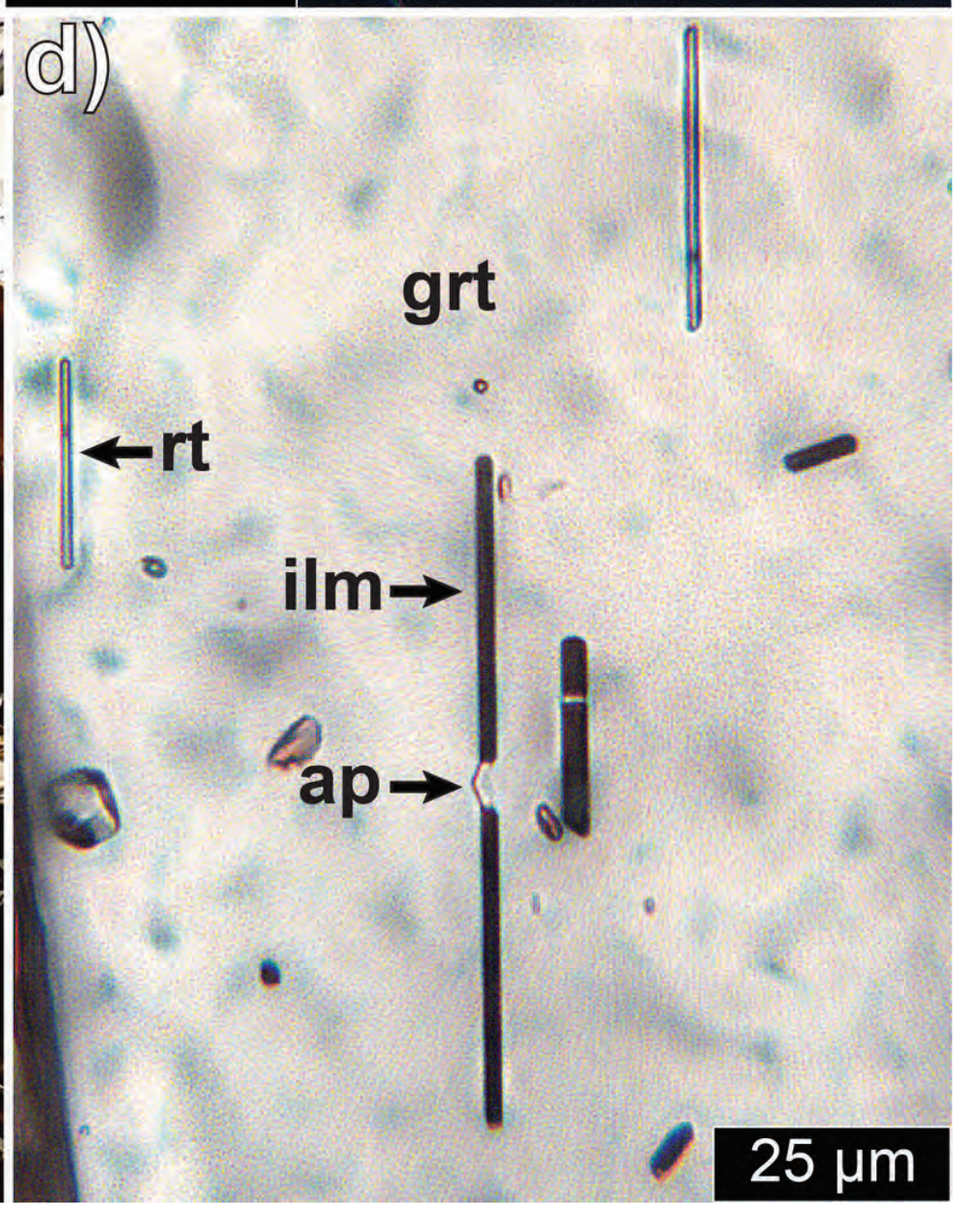
d)
grt
rt
ilm
ap
25 µm

Figure 5

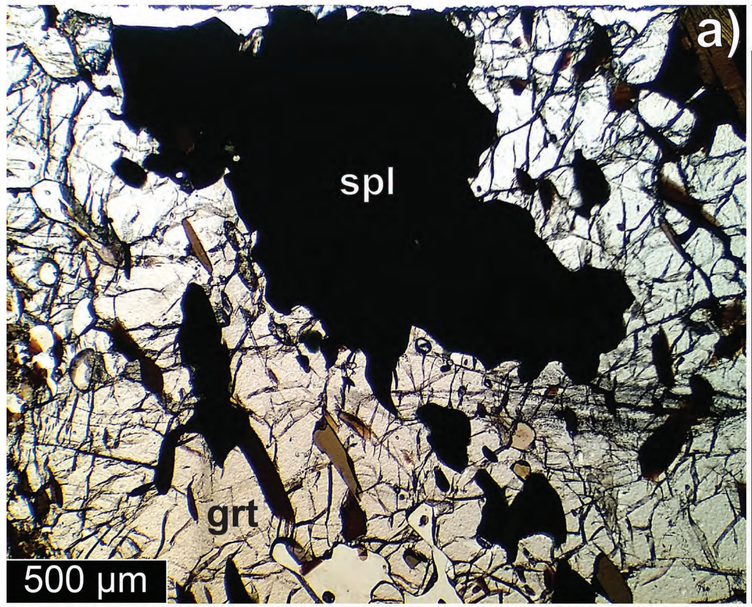
a)
spl
grt
500 µm

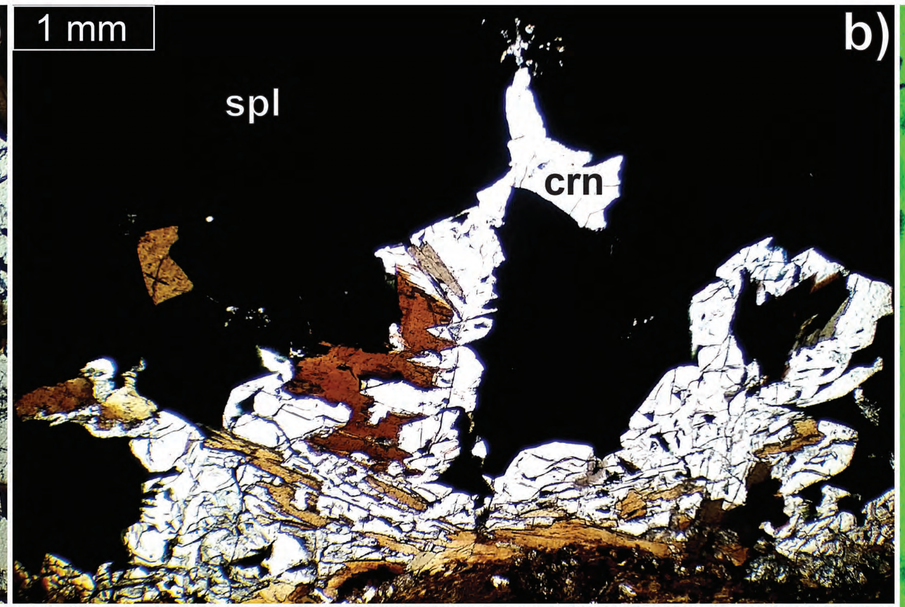
1 mm
b)
spl
crn

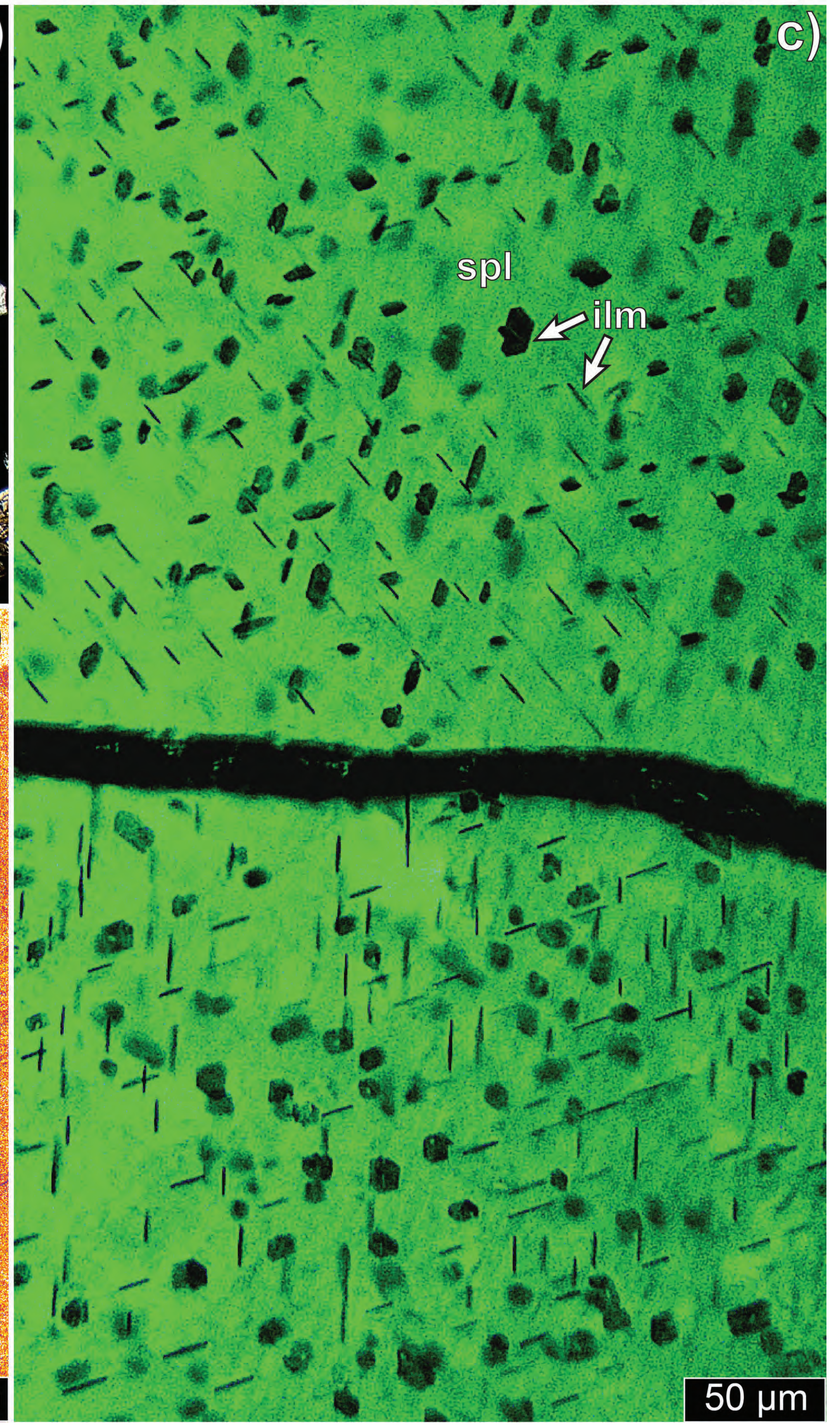
c)
spl
ilm
50 µm

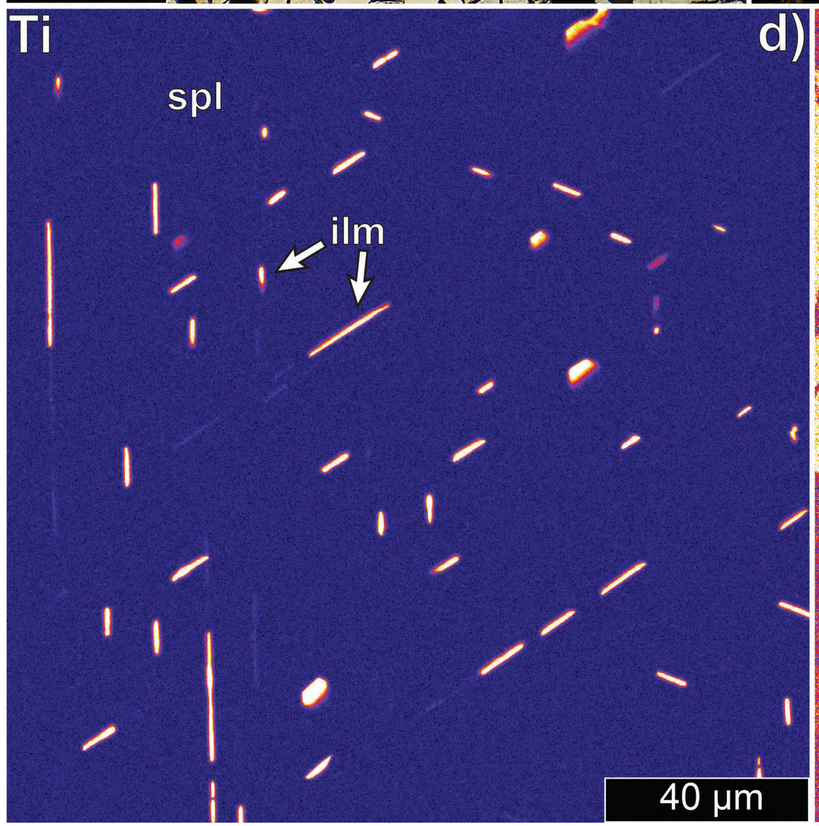
Ti
d)
spl
ilm
40 µm

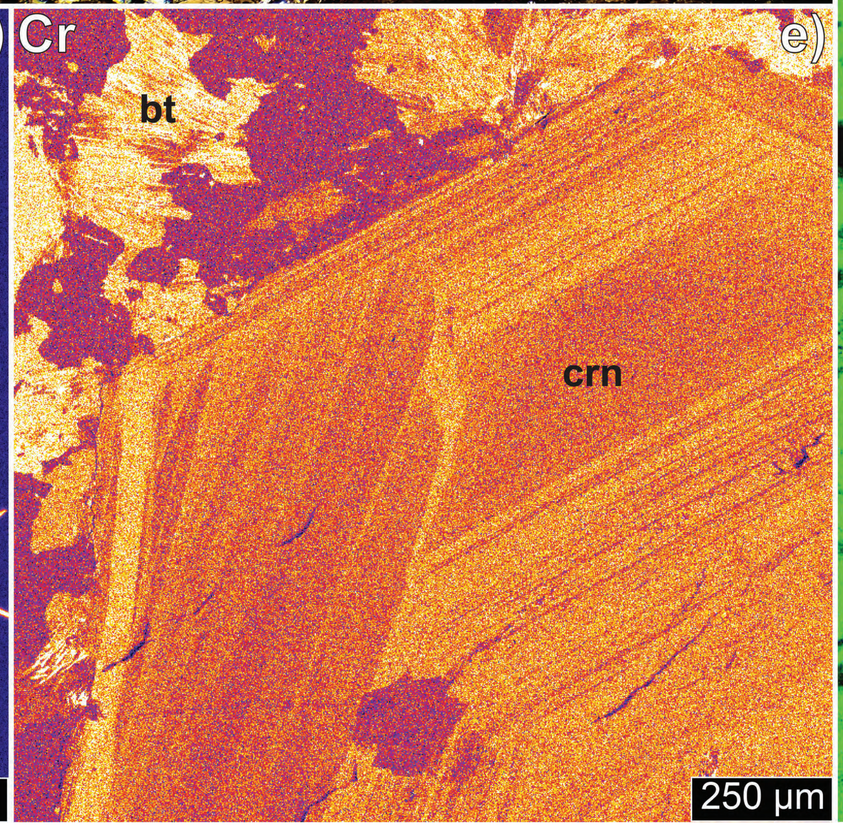
Cr
e)
bt
crn
250 µm

Figure 6

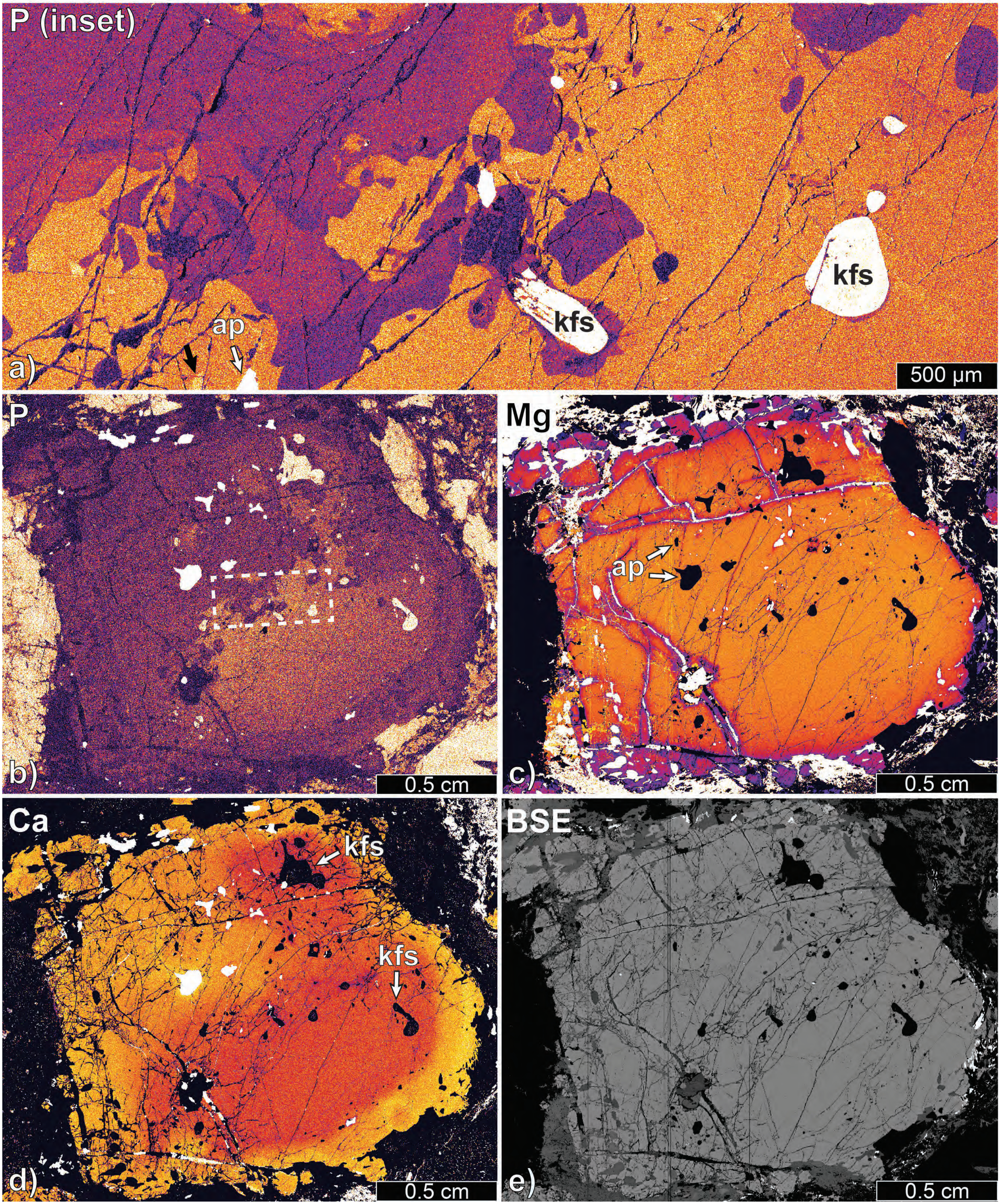
P (inset)
ap
kfs
kfs
a)
500 µm
P
b)
0.5 cm
Mg
ap
c)
0.5 cm
Ca
kfs
kfs
d)
0.5 cm
BSE
e)
0.5 cm

Figure 7

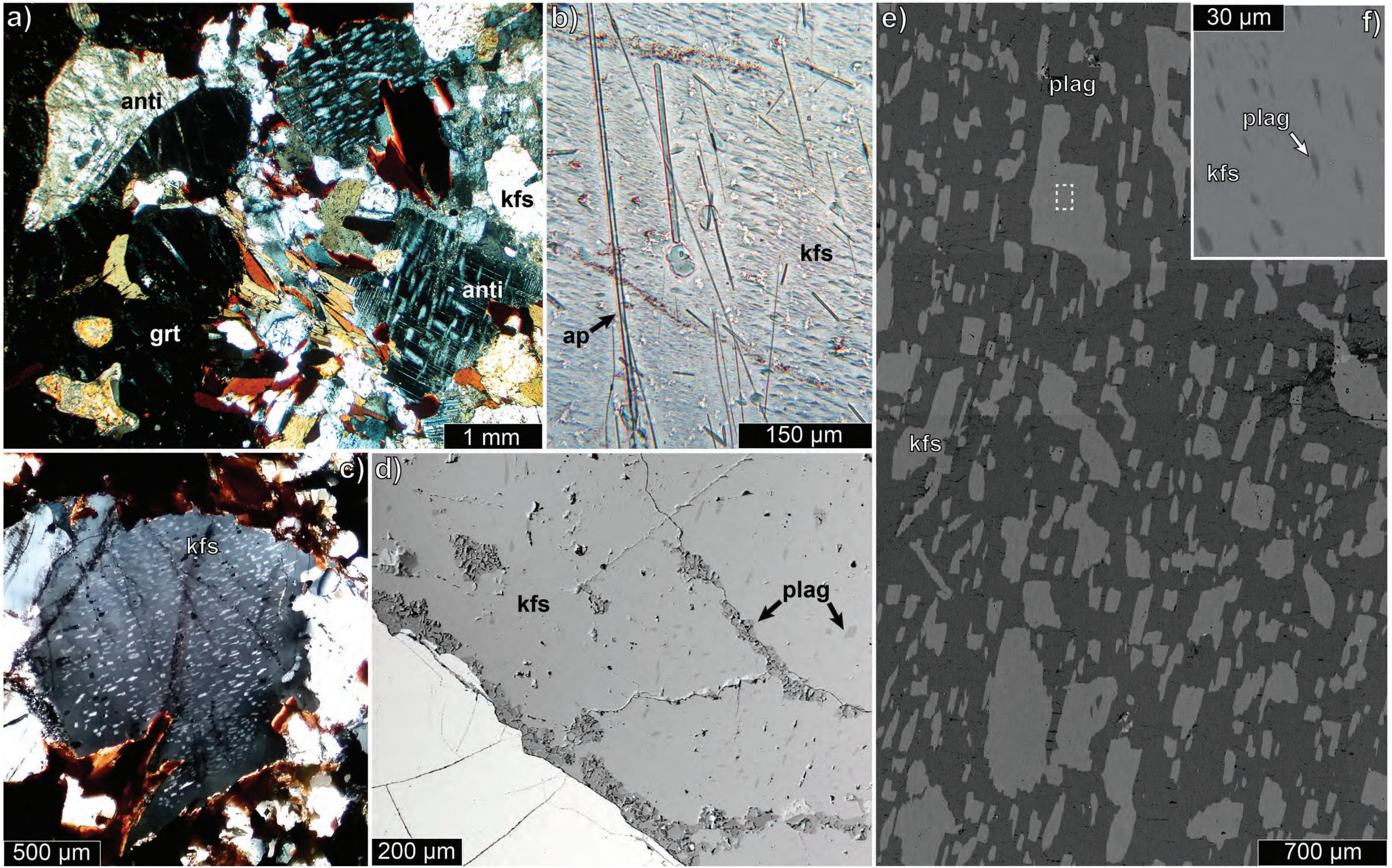
a)
anti
kfs
anti
grt
1 mm
b)
kfs
ap
150 µm
e)
plag
kfs
30 µm
f)
plag
kfs
700 µm
c)
kfs
500 µm
d)
kfs
plag
200 µm

Figure 8

Figure 9

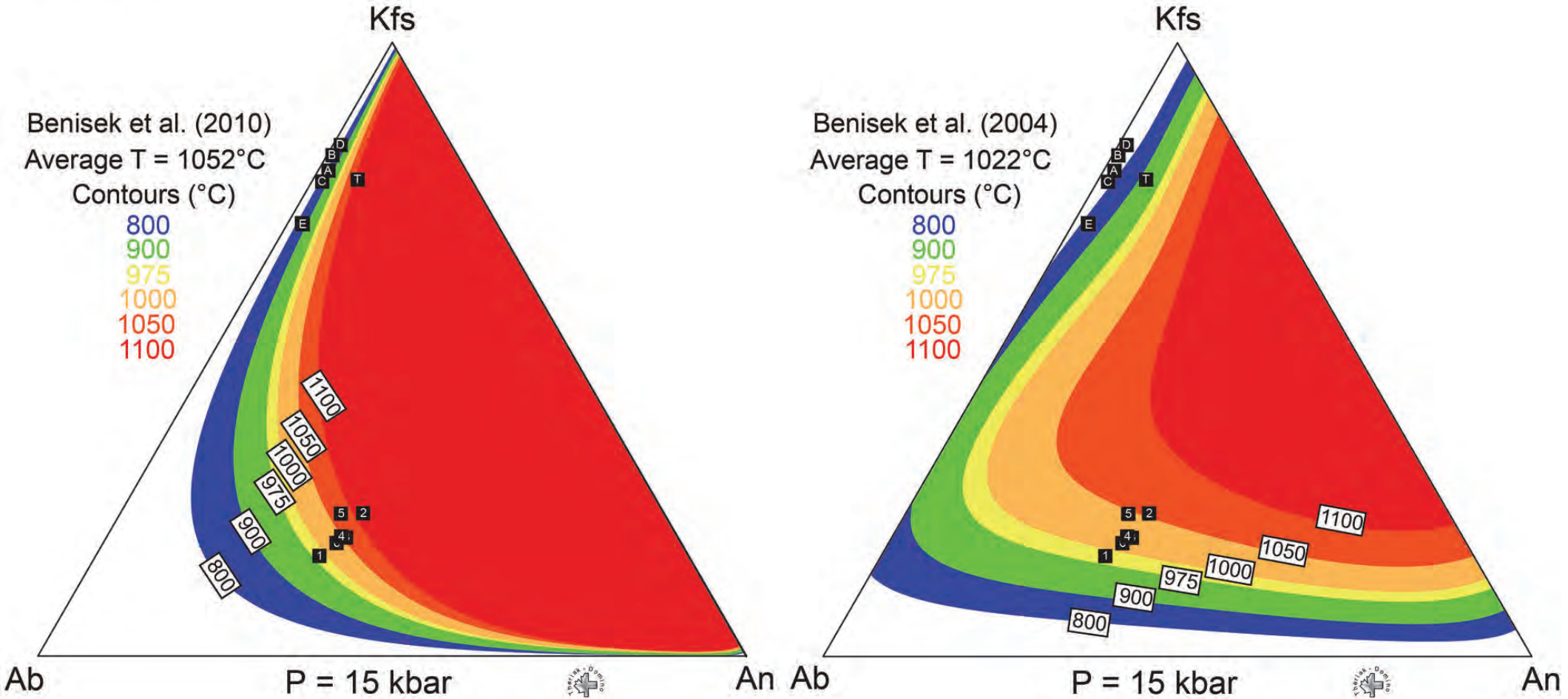
Kfs
Benisek et al. (2010)
Average T = 1052°C
Contours (°C)
800
900
975
1000
1050
1100
D
B
A
C
T
E
1100
1050
1000
975
900
800
5
2
4
1
Ab
P = 15 kbar
An
Kfs
Benisek et al. (2004)
Average T = 1022°C
Contours (°C)
800
900
975
1000
1050
1100
D
B
A
C
T
E
5
2
4
1
1100
1050
1000
975
900
800
Ab
P = 15 kbar
An

Figure 10

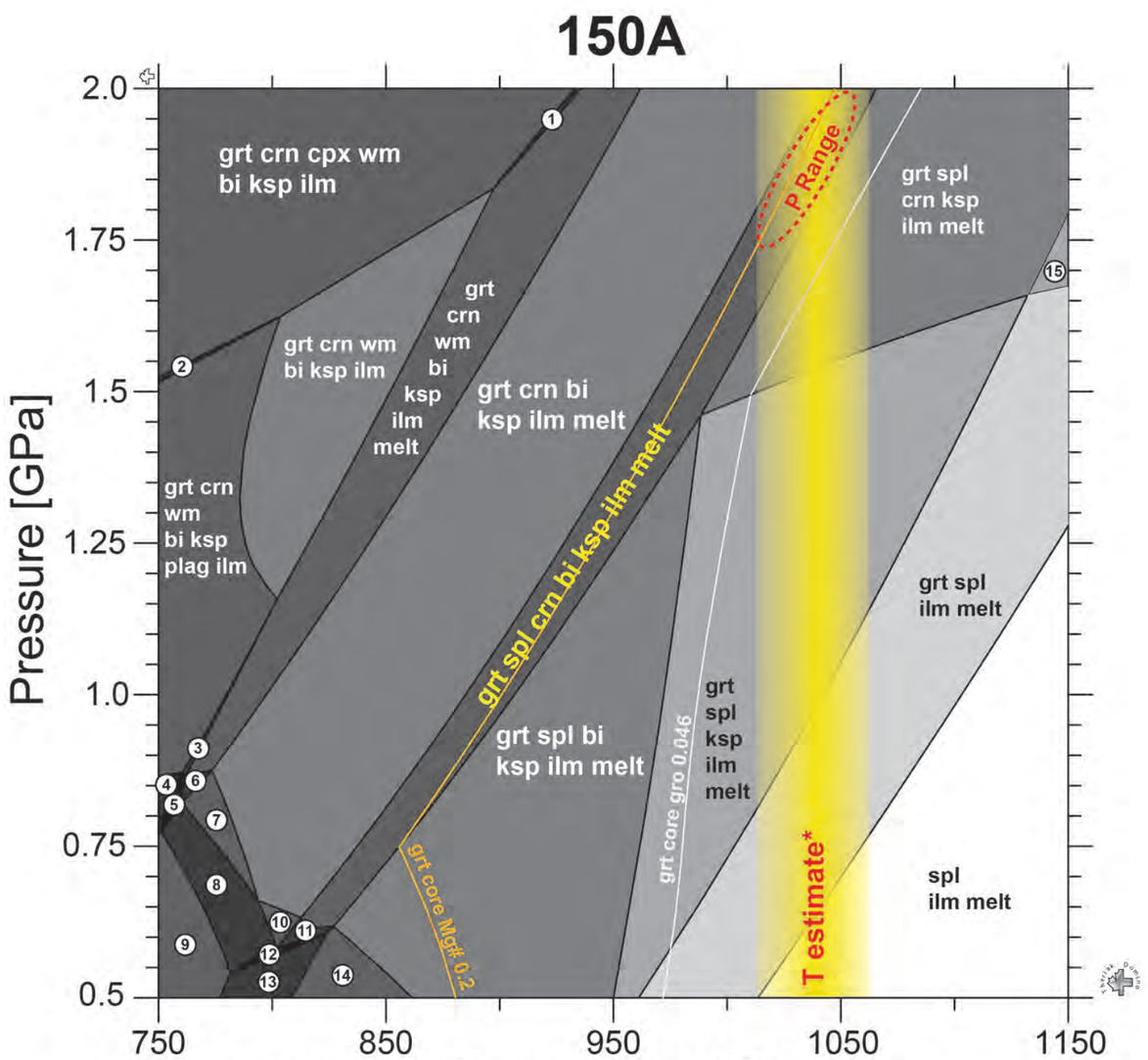

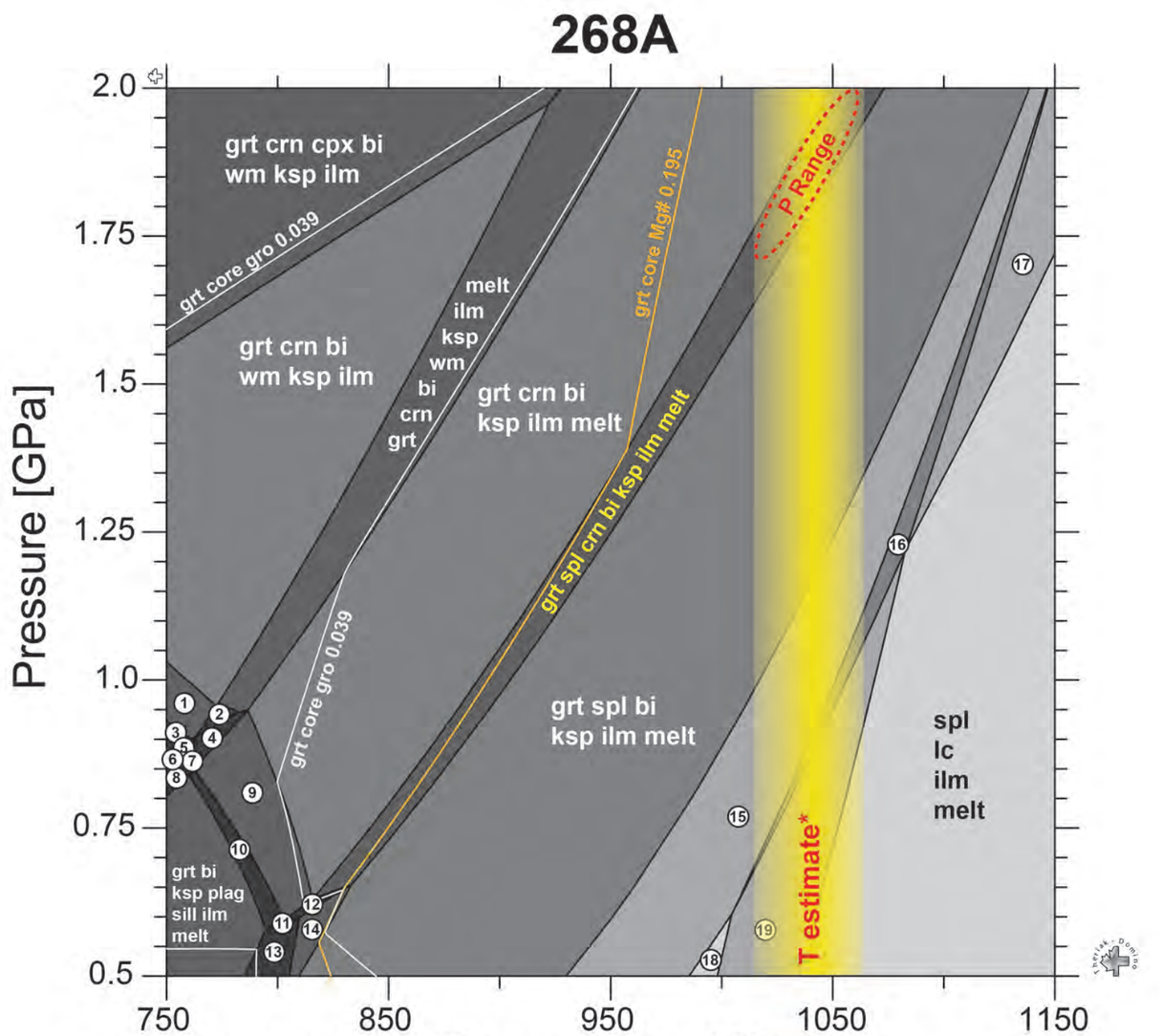

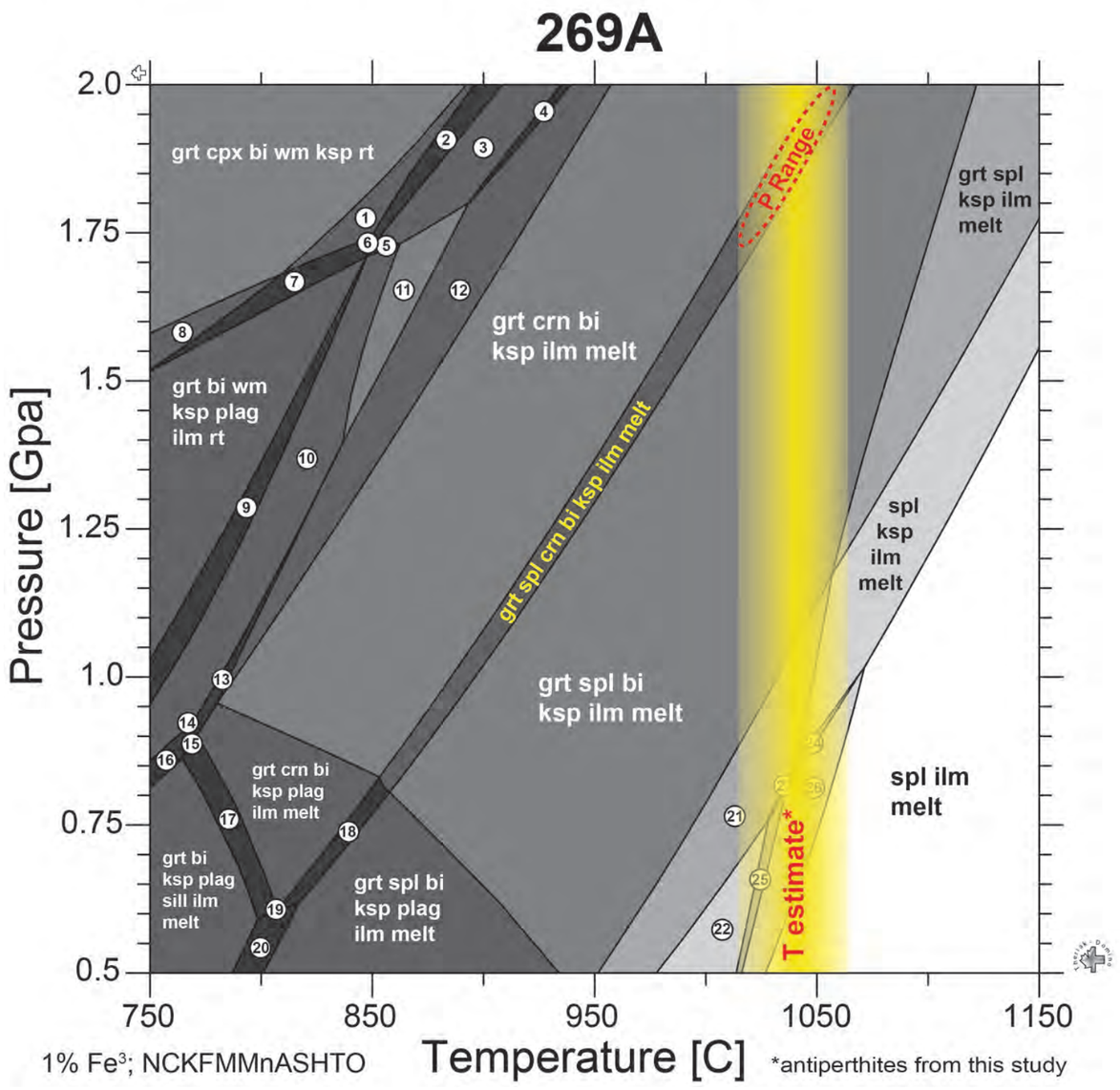

150A

1) grt crn cpx wm bi ksp ilm melt; 2) grt crn cpx wm bi ksp plag ilm; 3) grt crn wm bi ksp plag ilm melt
4) grt crn wm bi ksp plag sill ilm; 5) grt crn wm bi ksp plag sill ilm melt; 6) grt crn wm bi ksp sill ilm melt
7) grt crn bi ksp sill ilm melt; 8) grt crn bi ksp plag sill ilm melt; 9) grt bi ksp plag sill ilm melt
10) grt crn bi ksp plag ilm melt; 11) grt spl crn bi ksp plag ilm melt; 12) grt spl crn bi ksp plag sill ilm melt
13) grt spl bi ksp plag sill ilm melt; 14) grt spl bi ksp plag ilm melt; 15) grt spl crn ilm melt

268A

1) grt crn bi wm ksp ky ilm; 2) grt crn bi wm ksp ky ilm melt; 3) grt crn bi wm ksp plag ky ilm
4) grt crn bi wm ksp sill ilm melt; 5) grt crn bi wm ksp plag sill ilm; 6) grt bi wm ksp plag sill ilm
7) grt crn bi wm ksp plag sill ilm melt; 8) grt bi wm ksp plag sill ilm melt ; 9) grt crn bi ksp sill ilm melt
10) grt crn bi ksp plag sill ilm melt; 11) grt spl crn bi ksp plag sill ilm melt; 12) grt spl crn bi ksp sill ilm melt
13) grt spl bi ksp plag sill ilm melt; 14) grt spl bi ksp sill ilm melt; 15) spl bi ksp ilm melt
16) spl bi ksp lc ilm melt 17) spl ksp lc ilm melt; 18) spl bi ilm melt; 19) spl bi lc ilm melt

269A

1) grt cpx bi wm ksp ilm rt; 2) grt cpx bi wm ksp ilm rt melt; 3) grt cpx bi wm ksp ilm melt
4) grt crn cpx bi wm ksp ilm melt ; 5) grt cpx bi wm ksp plag ilm melt; 6) grt cpx bi wm ksp plag ilm melt
7) grt cpx bi wm ksp plag ilm rt; 8) grt cpx bi wm ksp plag rt; 9) grt bi wm ksp plag ilm rt melt
10) grt bi wm ksp plag ilm melt; 11) grt bi wm ksp ilm melt; 12) grt crn bi wm ksp ilm melt
13) grt crn bi wm ksp plag ilm melt; 14) grt bi wm ksp plag ky ilm melt
15) grt crn bi wm ksp plag sill ilm melt; 16) grt bi wm ksp plag sill ilm melt
17) grt crn bi ksp plag sill ilm melt; 18) grt spl crn bi ksp plag ilm melt
19) grt spl crn bi ksp plag sill ilm melt; 20) grt spl bi ksp plag sill ilm melt; 21) spl bi ksp ilm melt
22) spl bi ilm melt; 23) spl bi ksp lc ilm melt; 24) spl ksp lc ilm melt; 25) spl bi lc ilm melt
26) spl lc ilm melt